
**1 Local wind regime induced by giant linear dunes:
2 comparison of ERA5-Land re-analysis with surface
3 measurements**

**4 Cyril Gadal · Pauline Delorme ·
5 Clément Narteau · Giles F.S. Wiggs ·
6 Matthew Baddock · Joanna M. Nield ·
7 Philippe Claudin**

8
9 Received: DD Month YEAR / Accepted: DD Month YEAR

10 Abstract

11 Emergence and growth of sand dunes results from the dynamic interaction be-
12 tween topography, wind flow and sediment transport. While feedbacks between
13 these variables are well studied at the scale of a single dune, the average effect
14 of a periodic dune pattern on atmospheric flows remains poorly constrained
15 due to a lack of data in major sand seas. Here, we compare field measurements
16 of surface wind data to the predictions of the ERA5-Land climate reanalysis at
17 four locations in Namibia, including within the giant-dune field of the Namib
18 sand sea. In the desert plains to the north of the sand sea, observations and
19 predictions agree well. This is also the case in the interdune areas of the sand
20 sea, except for the weak winds blowing at night, which exhibit additional com-
21 ponents aligned with the giant dune orientation, which are not predicted by
22 the ERA5-Land reanalysis. We quantify these similarities and differences and

C. Gadal

Institut de Mécanique des Fluides de Toulouse, Université de Toulouse Paul Sabatier, CNRS,
Toulouse INP-ENSEEIHT, Toulouse, France. E-mail: cyril.gadal@imft.fr

P. Delorme

Energy and Environment Institute, University of Hull, Hull, UK.

C. Narteau

Institut de Physique du Globe de Paris, Université de Paris, CNRS, Paris, France.

G. Wiggs

School of Geography and the Environment, University of Oxford, Oxford, UK.

M. Baddock

Geography and Environment, Loughborough University, Loughborough, UK.

J.M. Nield

School of Geography and Environmental Science, University of Southampton, Southampton,
UK.

P. Claudin

Physique et Mécanique des Milieux Hétérogènes, CNRS, ESPCI Paris, PSL Research Uni-
versity, Université de Paris, Sorbonne Université, Paris, France.

23 provide a physical understanding of the relevant aerodynamical regimes to
24 relate them to the daily cycle of the turbulent atmospheric boundary layer
25 over a dune pattern of given wavelength. We conclude by identifying the con-
26 ditions under which the ERA5-Land reanalysis data can reliably be used to
27 study dune morphodynamics. We also propose that, in multidirectional wind
28 regimes, deflections of specific winds by giant dunes could explain the occur-
29 rence of secondary dune patterns with a different orientation to the primary
30 structures between which they develop.

31 **Keywords** Atmospheric boundary layer · Sand dunes · Fluid-structure
32 interactions

33 1 Introduction

34 The description of turbulent flows over complex topography is relevant for a
35 large variety of different environmental systems (Finnigan et al. 2020). For
36 example, the flow over hills is of primary interest for wind power, meteorolog-
37 ical and air pollution phenomena (Taylor et al. 1987). The properties of
38 these flows are also key to the understanding of geophysical phenomena, in-
39 cluding the formation of wind-driven waves on the ocean surface (Sullivan and
40 McWilliams 2010), dissolution bedforms (Claudin et al. 2017), or sedimentary
41 ripples and dunes (Charru et al. 2013; Courrech du Pont 2015). Importantly,
42 the troposphere presents a vertical structure, with a lower convective bound-
43 ary layer, of typical kilometer-scale thickness, capped by a stably stratified
44 region (Stull 1988). The largest topographic obstacles, such as mountains, can
45 therefore interact with this upper region and lead to internal wave generation
46 or significant wind disturbances, such as lee-side downslope winds (Durran
47 1990).

48 Focusing on the wind close to the surface, two related topographic feed-
49 backs on the windflow over dunes can be commented on separately. First is
50 the effect on wind speed, with documented flow acceleration on upwind slopes
51 (Weaver and Wiggs 2011) and deceleration on downwind slopes (Baddock et al.
52 2007), where the speed-up factor is essentially proportional to the obstacle as-
53 pect ratio (Jackson and Hunt 1975). Importantly, the velocity maximum is
54 typically shifted upwind of the obstacle crest. This behaviour has been the-
55oretically predicted by means of asymptotic analysis of a neutrally stratified
56 boundary-layer flow over an obstacle of vanishing aspect ratio (Jackson and
57 Hunt 1975; Mason and Sykes 1979; Sykes 1980; Hunt et al. 1988; Belcher and
58 J.C.R. 1998). Experiments in flumes (Zilker et al. 1977; Zilker and Hanratty
59 1979; Frederick and Hanratty 1988; Poggi et al. 2007; Bristow et al. 2022),
60 in wind tunnels (Gong and Ibbetson 1989; Finnigan et al. 1990; Gong et al.
61 1996) and in field conditions (Taylor and Teunissen 1987; Claudin et al. 2013;
62 Fernando et al. 2019; Lü et al. 2021), have also documented this effect. In-
63 terestingly, a similar behaviour exists for the pressure perturbation, but with
64 a slight downwind shift for the pressure minimum (Claudin et al. 2021). The
65 second effect, much less studied, is the flow deflection that occurs when the
66 incident wind direction is not perpendicular to the ridge crest. While predicted
67 to be small (less than 10°) in the linear regime valid for shallow topography
68 (Gadal et al. 2019), significant flow steering has been reported in the field on
69 the downwind side of steep enough obstacles, such as mountain ranges (Kim
70 et al. 2000; Lewis et al. 2008; Fernando et al. 2019), well-developed sand dunes
71 (Walker et al. 2009; Hesp et al. 2015; Walker et al. 2017; Smith et al. 2017; de
72 Winter et al. 2020), and valley topographies (Wiggs et al. 2002; Garvey et al.
73 2005).

74 For practical reasons, wind measurement over sand dunes has been per-
75 formed over small bedforms, typically a few meters high (corresponding to
76 tens of meters long) (e.g. Lancaster et al. (1996), Mckenna Neuman et al.
77 (1997), Sauermann et al. (2003), Andreotti et al. (2002), Walker and Nick-

ling (2002), Weaver and Wiggs (2011)). Giant dunes, with kilometer-scale wavelengths and heights of tens of meters, are more difficult to investigate although for several reasons they provide a choice configuration for the study of turbulent flows over a complex topography. First, one expects larger wind disturbances for larger obstacles. Secondly, their large size makes them interact with the vertical structure of the atmosphere (Andreotti et al. 2009). Third, they usually form large patterns in sand seas and thus behave as rather clean periodic perturbations, in contrast with isolated dunes. Finally, because the morphodynamics of aeolian bedforms are strongly dependent on the local wind regime (Livingstone and Warren 2019), one can expect to see the consequences of windflow disturbance by large dunes on neighbouring small dunes. A similar effect is observed on the properties of impact ripple patterns due to the presence of dunes (Howard 1977; Hood et al. 2021).

Atmospheric flows have been much studied at the desert-scale with climate reanalyses based on global atmospheric models (Blumberg and Greeley 1996; Livingstone et al. 2010; Ashkenazy et al. 2012; Jolivet et al. 2021; Hu et al. 2021), such as ERA-40, ERA-Interim or ERA-5 (Uppala et al. 2005; Dee et al. 2011; Hersbach et al. 2020). However, the spatial resolution (tens of kilometers) of these reanalyses implies average quantities that do not resolve the smaller scales of interest, which range from individual dunes to small mountains (Livingstone et al. 2010). Recently, the release of ERA5-Land has resolved this limitation by providing up to 70 years of hourly wind predictions at a 9 km spatial resolution (Muñoz-Sabater et al. 2021). However, its validity remains to be studied, especially in remote desert areas where assimilation of measured data is very low.

In this work, we compare local wind speeds and directions measured by meteorological stations at four different locations inside and north of the giant-dune field of the Namib sand sea to the regional predictions of the ERA5-Land climate reanalysis. Where the meteorological stations are surrounded by a relatively flat environment, we show that local measurements and regional predictions agree well. The agreement is also good in the interdune areas of the sand sea, except for some weak winds blowing at night, which exhibit an additional component aligned with the giant dune orientation. These winds are not predicted by the ERA5-Land reanalysis (section 2). Further, we are able to link the magnitude of these differences to the circadian cycle of the atmospheric boundary layer (section 3). Finally, we draw implications for the wind disturbances on smaller-scale dunes (section 4), suggesting a possible origin for crossing dunes.

116 2 Wind regimes across the Namib Sand Sea

117 We measured the wind regime at four different locations in Namibia, representative
118 of various arid environments across the Namib desert (Fig. 1, Fig. 2).
119 The Etosha West station was located at the Adamax waterhole to the west
120 of Etosha Pan in northern Namibia, in a sparsely vegetated area. The Huab

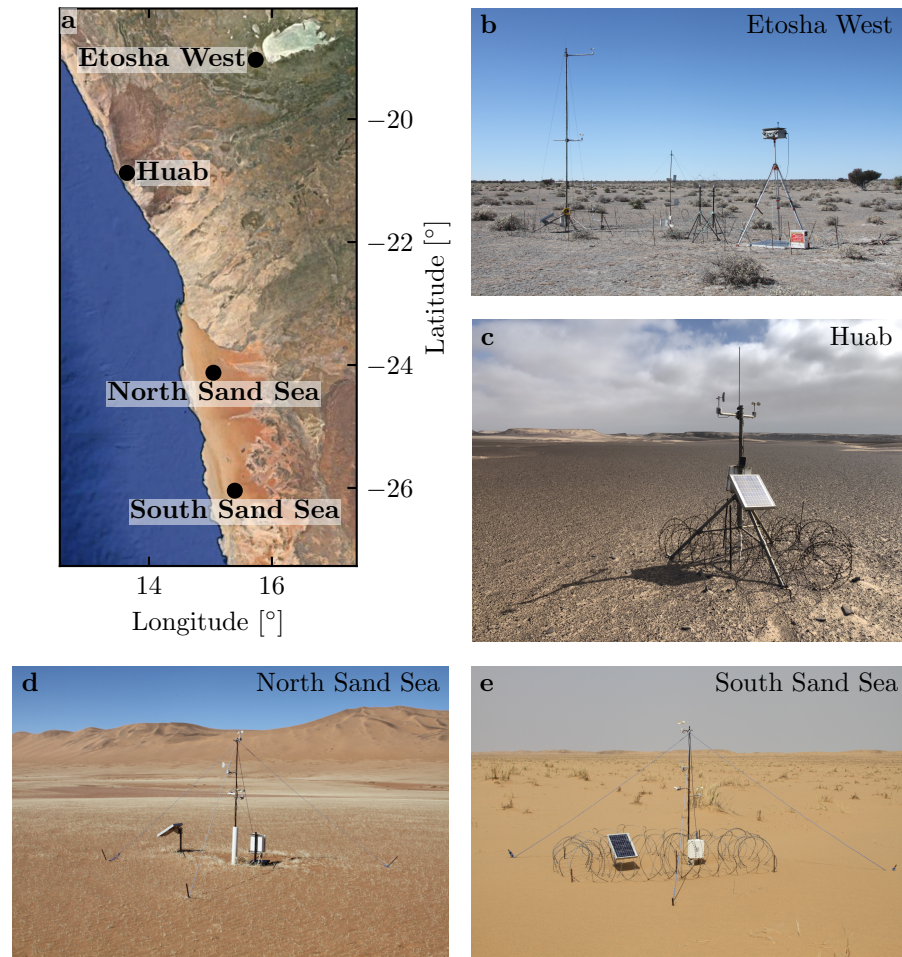


Fig. 1 Studied field sites. **a:** Location of the different sites in Namibia. **b–e:** Photographs of the meteorological stations.

station was near the coast on a hyper-arid flat gravel plain lying north the ephemeral Huab river. Here, barchan dunes up to a few meters in height develop from the sediment blowing out of the river valley (Nield et al. 2017; Hesp and Hastings 1998). These two stations were both located in relatively flat environments. In contrast, the North Sand Sea and South Sand Sea stations were located in the interdunes between linear dunes with kilometer-scale wavelengths, hectometer-scale heights and superimposed patterns. In this section, we describe and compare winds from local measurements and climate reanalysis predictions.

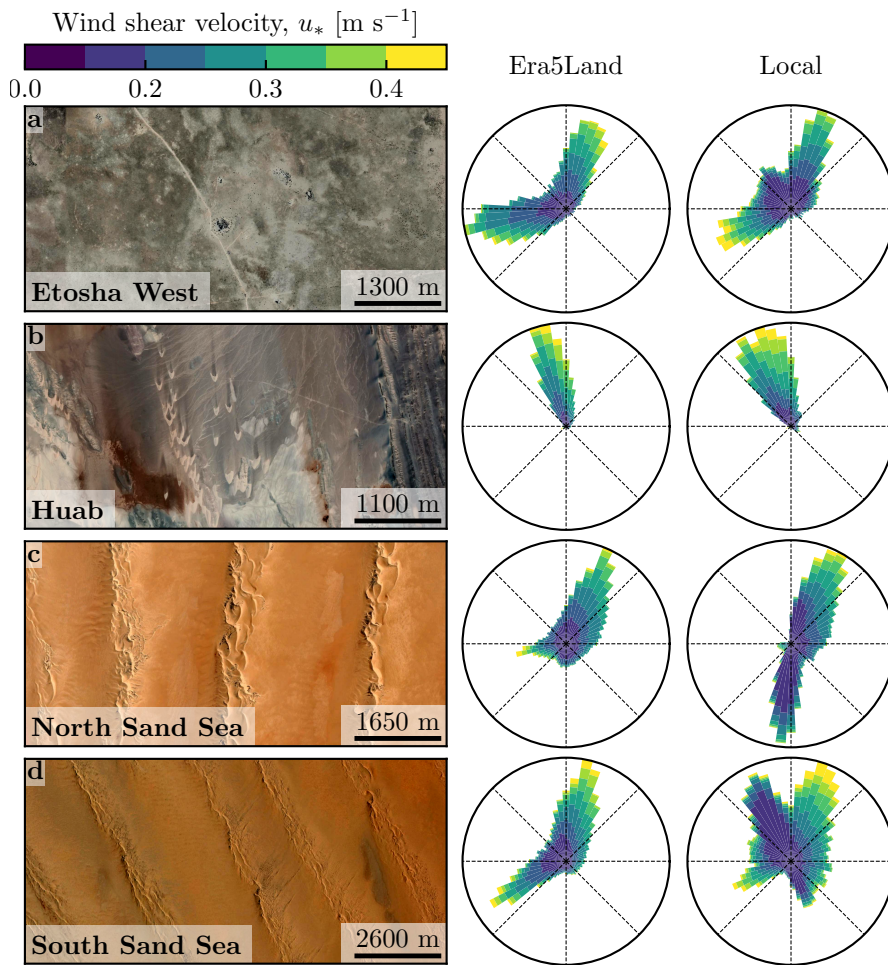


Fig. 2 Wind data used in this study. Satellite images of these different environments (Google-Earth, Maxar Technologies, CNES/Airbus) are shown on the left. The black dots show the location of the wind measurements stations. On the center and on the right, wind roses representing the data from the ERA5-Land climate reanalysis and the local wind stations are respectively shown. Note that the bars show the direction towards which the wind blows.

130 2.1 Wind and elevation data

131 At each meteorological station (Fig. 1), wind speed and direction were sampled
 132 every 10 minutes using cup anemometers (Vector Instruments A100-LK) and
 133 wind vanes (Vector Instruments W200-P) at heights which varied between 2 m
 134 and 3 m depending on the station. The available period of measurements at
 135 each station ranged from 1 to 5 discontinuous years distributed between 2012
 136 and 2020 (Online Resource Fig. S1). We checked that at least one complete

137 seasonal cycle was available for each station. Regional winds were extracted
138 at the same locations and periods from the ERA5-Land dataset, which is a
139 replay at a smaller spatial resolution of ERA5, the latest climate reanalysis
140 from the ECMWF (Hersbach et al. 2020; Muñoz-Sabater et al. 2021). This
141 dataset provided hourly predictions of the 10-m wind velocity and direction
142 at a spatial resolution of $0.1^\circ \times 0.1^\circ$ (≈ 9 km in Namibia).

143 To enable direct comparison, the local wind measurements were averaged
144 into 1-hr bins centered on the temporal scale of the ERA5-Land estimates
145 (Online Resource Fig. S2). As the wind velocities of both datasets were pro-
146 vided at different heights, we converted them into shear velocities u_* (Online
147 Resource section 1), characteristic of the turbulent wind profile. Wind roses
148 in Fig. 2 show the resulting wind data.

149 Dune properties were computed using autocorrelation on the 30-m Digital
150 Elevation Models (DEMs) of the shuttle radar topography mission (Farr et al.
151 2007). For the North and South Sand Sea stations, we obtain, respectively,
152 orientations of 85° and 125° with respect to the North, wavelengths of 2.6 km
153 and 2.3 km and amplitudes (or half-heights) of 45 m and 20 m (Online Resource
154 Fig. S4 for more details). This agrees with direct measurements made on site.

155 2.2 Comparison of local and regional winds

156 The measured and predicted wind regimes are shown in Fig. 2. In the Namib,
157 the regional wind patterns are essentially controlled by the sea breeze, result-
158 ing in strong northward components (sometimes slightly deviated by the large
159 scale topography) present in all regional wind roses (Lancaster 1985). These
160 daytime winds are dominant during the period October-March (Fig. 3f and
161 Online Resource Fig. 4f). During April-September, an additional (and often
162 nocturnal) easterly component can also be recorded, induced by the combina-
163 tion of katabatic winds forming in the mountains, and infrequent ‘berg’ winds,
164 which are responsible for the high wind velocities observed (Lancaster et al.
165 1984). The frequency of these easterly components decreases from inland to
166 the coast. As a result, bidirectional wind regimes within the Namib Sand Sea
167 and at the west Etosha site (Fig. 2a,c,d) and a unidirectional wind regime on
168 the coast at the outlet of the Huab River (Fig. 2b) are observed.

169 In the case of the Etosha West and Huab stations, the time series of wind
170 speed and direction from the regional predictions quantitatively match those
171 corresponding to the local measurements (Figs. 3, 4 and Online Resource
172 Fig. S5). For the North Sand Sea and South Sand Sea stations within the
173 giant dune field, we observe that this agreement is also good, but limited to
174 the October-March time period (Fig. 4a, b, e, f). However, the field-measured
175 wind roses exhibit additional wind components aligned with the giant dune
176 orientation, as evidenced on the satellite images (Fig. 2c,d).

177 More precisely, during the April-September period, the local and regional
178 winds in the interdune match during daytime only, i.e when the southerly/southwesterly
179 sea breeze dominates (Figs. 5c,d,g,h and 6). In the late afternoon and during

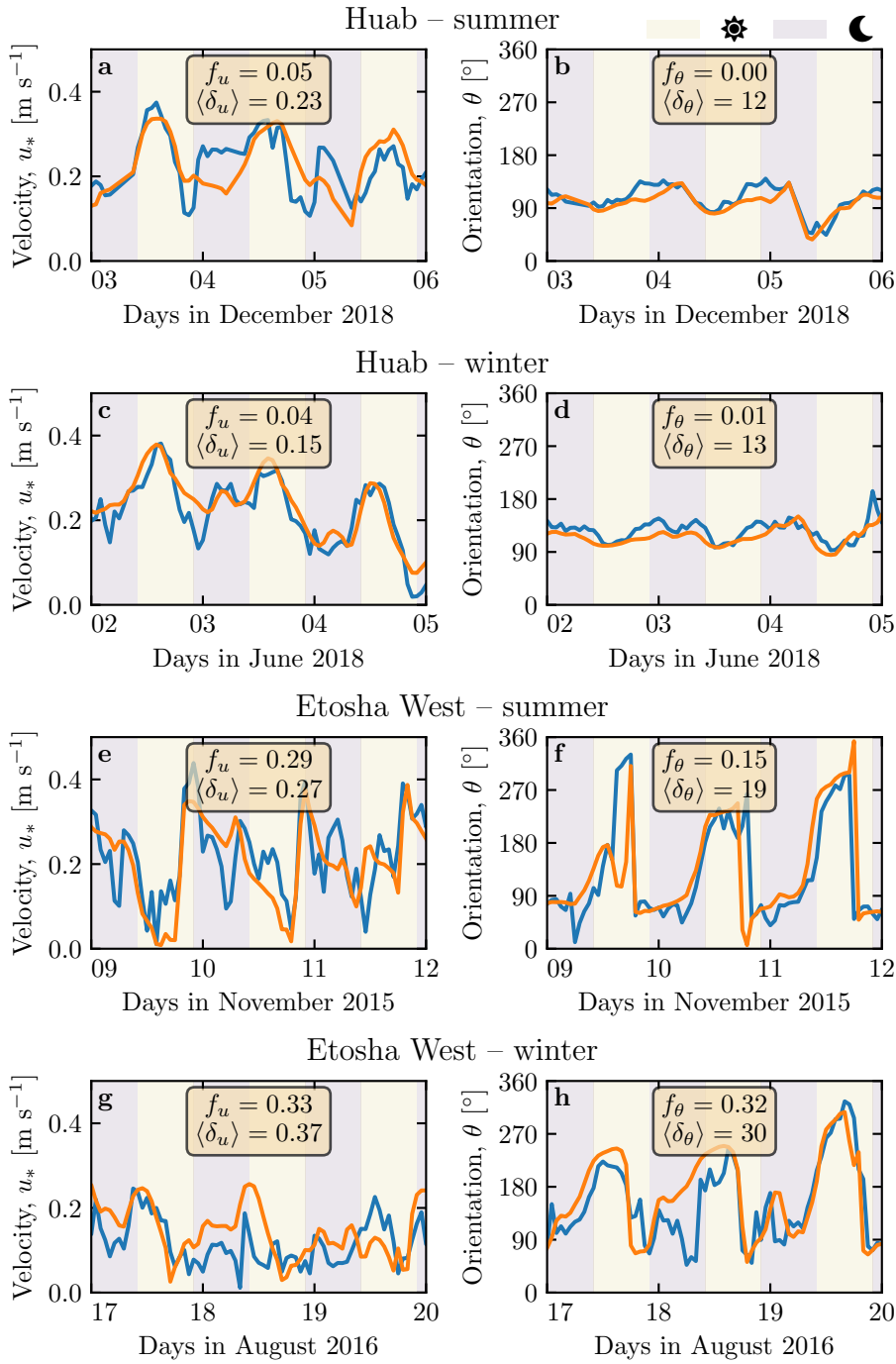


Fig. 3 Temporal comparison between the wind data coming from the ERA5-Land climate reanalysis (orange lines) and from the local measurements (blue lines). Coloured swathes indicate day (between 1000 UTC and 2200 UTC) and night (before 1000 UTC or after 2200 UTC). **a–b:** Etosha West station in summer. **b–c:** Etosha West station in winter. **d–e:** Huab station in summer. **f–g:** Huab station in winter. Time series of the two other stations are shown in Fig. 5.

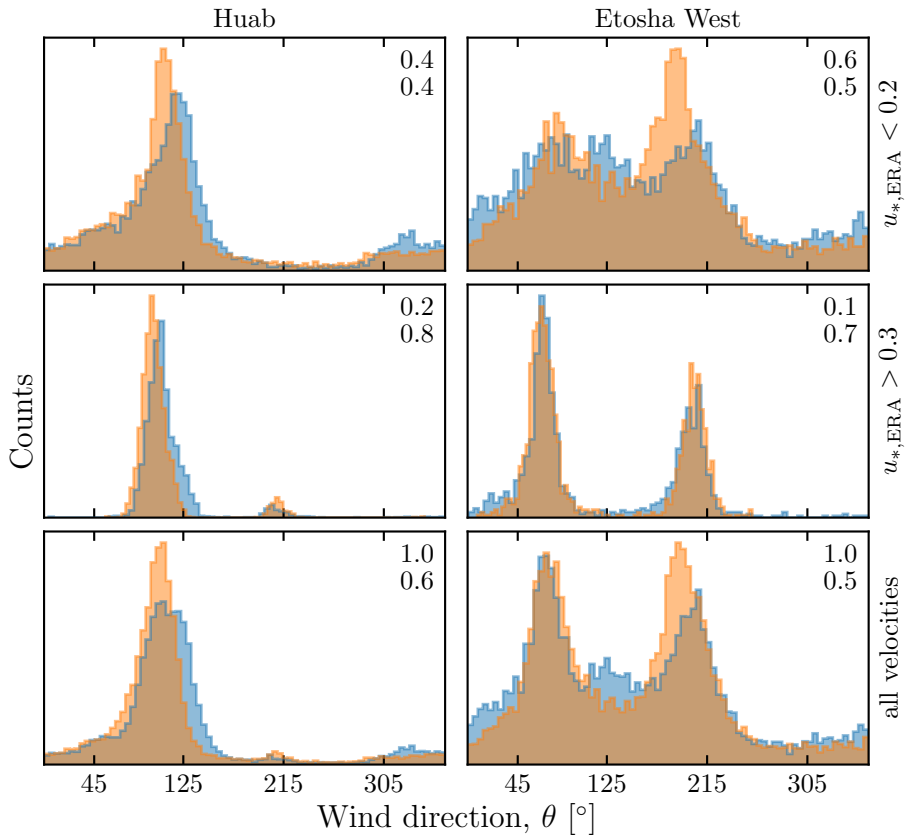


Fig. 4 Distributions of wind direction at the Huab and Etosha West stations for the ERA5-Land climate reanalysis (orange) and the local measurements (blue). In each subplot, both distributions are plotted from the same time steps, selected with constraints on the wind wind velocity (rows) in the ERA5-Land dataset. The numbers at the top centre give the percentage of time steps selected in each sub-range, as well as the percentage of them corresponding to the day (between 1000 UTC and 2200 UTC).

180 the night, when the easterly ‘berg’ and katabatic winds blow, measurements
 181 and predictions differ. In this case, the angular wind distribution of the local
 182 measurements exhibits two additional modes corresponding to reversing winds
 183 aligned with the giant dune orientation (purple frame in Fig. 6, Online Re-
 184 source Fig. S6). This deviation is also associated with a general attenuation
 185 of the wind strength (Online Resource Fig. S7). Remarkably, all these figures
 186 show that these wind reorientation and attenuation processes occur only at
 187 low velocities of the regional wind, typically for $u_{*,\text{ERA}} \lesssim 0.2 \text{ m s}^{-1}$. For
 188 shear velocities larger than $u_{*,\text{ERA}} \simeq 0.3 \text{ m s}^{-1}$, the wind reorientation is not
 189 apparent. Finally, for intermediate shear velocities, both situations of wind
 190 flow reoriented along the dune crest and not reoriented can be successively
 191 observed (Online Resource Fig. S6). Importantly, these values are not pre-

¹⁹² cise thresholds, but indicative of a crossover between regimes, whose physical
¹⁹³ interpretation is discussed in the next section.

¹⁹⁴ **3 Influence of wind speed and circadian cycle on the atmospheric
¹⁹⁵ boundary layer**

¹⁹⁶ The wind deflection induced by linear dunes has previously been related to the
¹⁹⁷ incident angle between wind direction and crest orientation, with a maximum
¹⁹⁸ deflection evident for incident angles between 30° and 70° (Walker et al. 2009;
¹⁹⁹ Hesp et al. 2015). In the data analysed here, the most deflected wind at both
²⁰⁰ the North and South Sand Sea stations is seen to be where the incident angle
²⁰¹ is perpendicular to the giant dunes (Figs. 2 and 6). It therefore appears that
²⁰² in our case, the incident wind angle is not the dominant control on maximum
²⁰³ wind deflection. Further, and as shown in Fig. 6, winds of high and low veloc-
²⁰⁴ ities show contrasting behaviour in characteristics of deflection. This suggests
²⁰⁵ a change in hydrodynamical regime between the winds. In this section, we
²⁰⁶ discuss the relevant parameters associated with the dynamical mechanisms
²⁰⁷ that govern the interactions between the atmospheric boundary layer flow and
²⁰⁸ giant dune topographies. This analysis allows us to provide a physics-based
²⁰⁹ interpretation of our measured wind data.

²¹⁰ **3.1 Flow over a modulated bed**

²¹¹ Taking as a reference the turbulent flow over a flat bed, the general framework
²¹² of our study is understanding and describing the flow response to a bed mod-
²¹³ ulation (e.g. a giant dune). Without loss of generality, we can consider in this
²¹⁴ context an idealised bed elevation in the form of parallel sinusoidal ridges, with
²¹⁵ wavelength λ (or wavenumber $k = 2\pi/\lambda$) and amplitude ξ_0 , and where the ref-
²¹⁶ erence flow direction makes a given incident angle with respect to the ridge
²¹⁷ crest (Andreotti et al. 2012). Part of this response, on which we focus here,
²¹⁸ is the flow deflection by the ridges. In a simplified way, it can be understood
²¹⁹ from the Bernoulli principle (Hesp et al. 2015): as the flow approaches the
²²⁰ ridge crest, the compression of the streamlines results in larger flow velocities,
²²¹ and thus lower pressures (Rubin and Hunter 1987). An incident flow oblique
²²² to the ridge is then deflected towards lower pressure zones, i.e towards the
²²³ crest. Turbulent dissipation tends to increase this effect downstream, resulting
²²⁴ in wind deflection along the crest in the lee side (Gadal et al. 2019).

²²⁵ Flow confinement below a capping surface, which enhances streamline com-
²²⁶ pression, has a strong effect on the hydrodynamic response and typically in-
²²⁷ creases flow deflection. This is the case for bedforms forming in open channel
²²⁸ flows such as rivers (Fourrière et al. 2010; Unsworth et al. 2018). This is also
²²⁹ relevant for aeolian dunes as they evolve in the turbulent atmospheric bound-
²³⁰ ary layer (ABL) capped by the stratified free atmosphere (FA) (Andreotti
²³¹ et al. 2009). Two main mechanisms, associated with dimensionless numbers

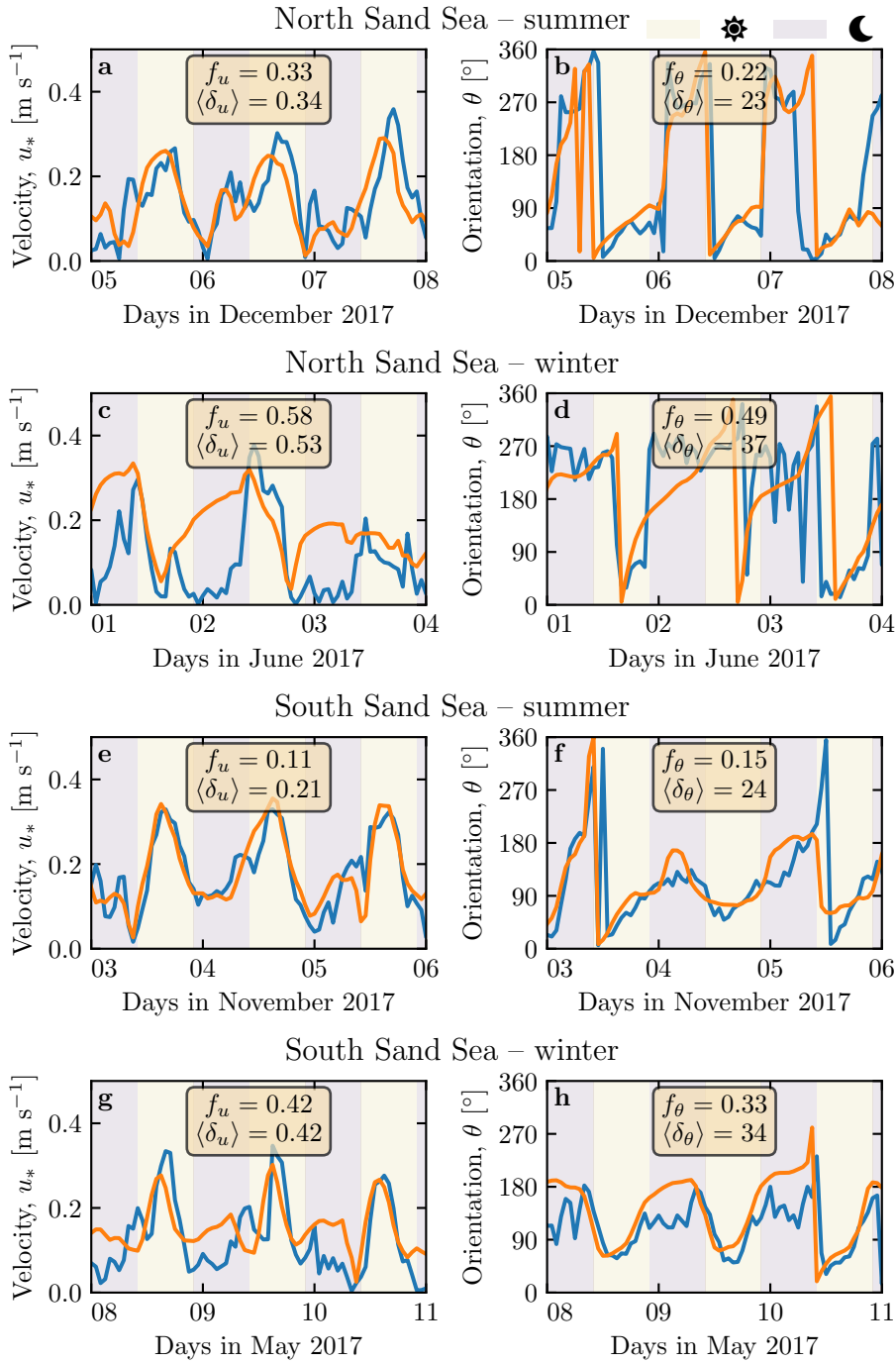


Fig. 5 Temporal comparison between the wind data coming from the ERA5-Land climate reanalysis (orange lines) and from the local measurements (blue lines). Coloured swathes indicate day (between 1000 UTC and 2200 UTC) and night (before 1000 UTC or after 2200 UTC). **a–b:** North Sand Sea station in summer. **b–c:** North Sand Sea station in winter. **d–e:** South Sand Sea in summer. **f–g:** South Sand Sea station in winter. Time series of the two other stations are shown in Fig. 3.

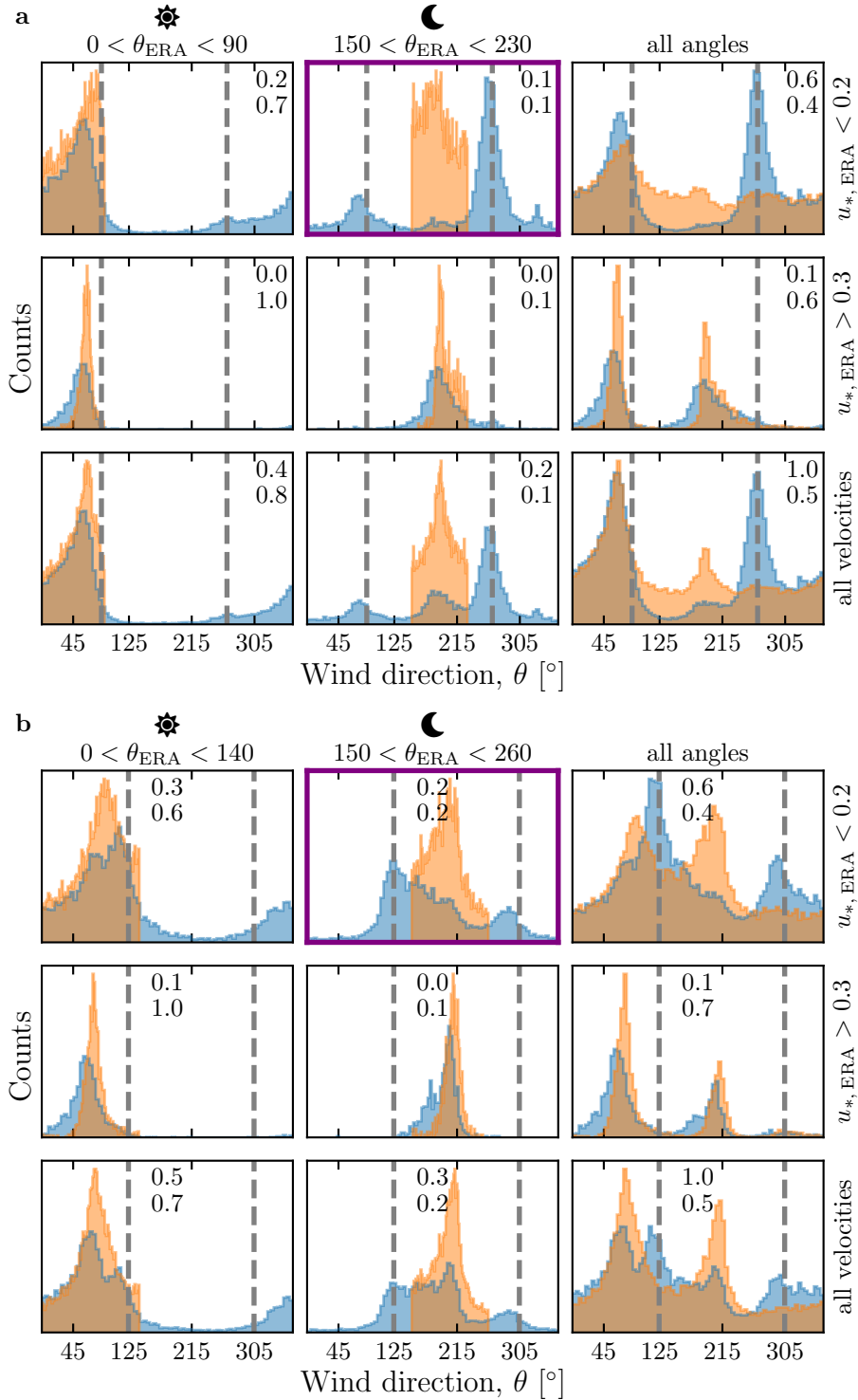


Fig. 6 Distributions of wind direction at the North Sand Sea (**a**) and South Sand Sea (**b**) stations for the ERA5-Land climate reanalysis (orange) and the local measurements (blue). In each subplot, both distributions are plotted from the same time steps, selected with constraints on the wind direction (columns) and/or wind velocity (rows) of the ERA5-Land dataset. The grey vertical dashed lines indicate the dune orientation. The numbers at the top right give the percentage of time steps selected in each sub-range, as well as the percentage corresponding to the daytime (between 1000 UTC and 2200 UTC). Contrary to the Huab and Etosha West stations (Fig. 4), histograms does not match low wind velocities. More specifically, the purple frame highlights the regime (low wind velocities, nocturnal easterly wind) in which the data from both datasets differ.

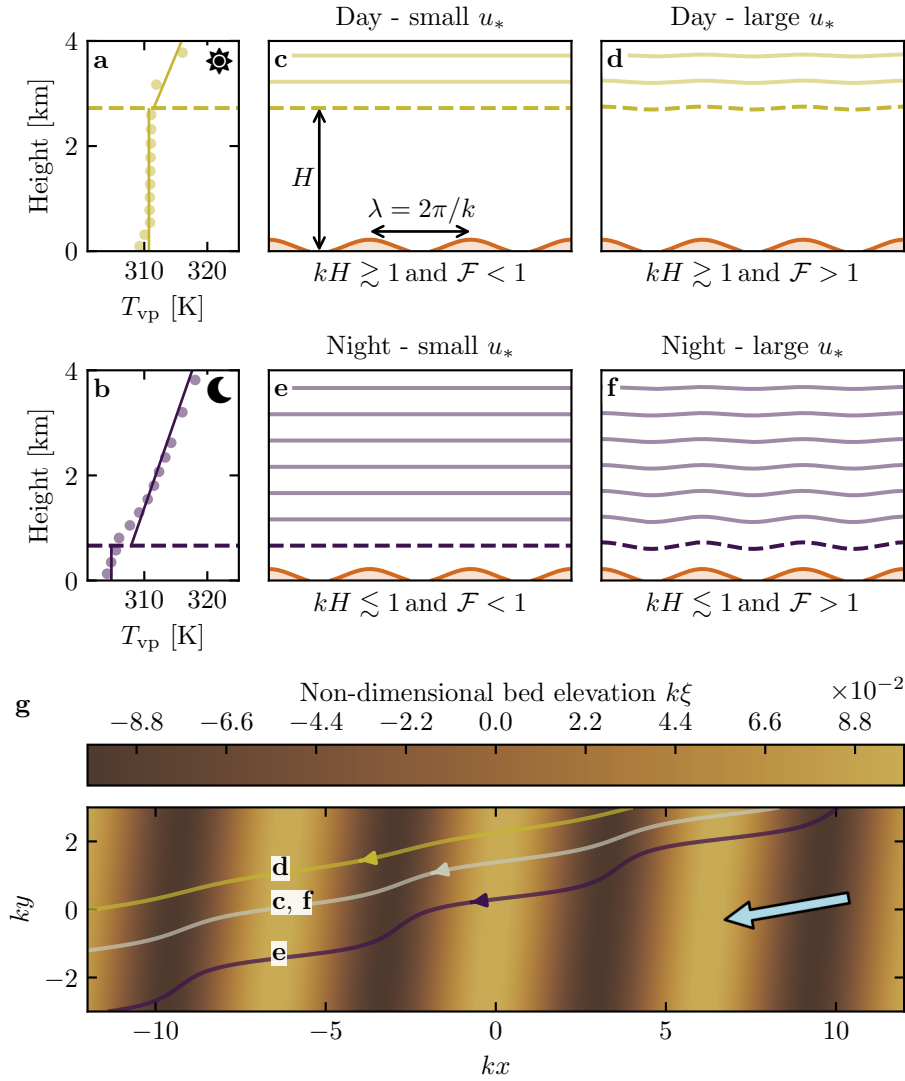


Fig. 7 **a–b:** Vertical profiles of the virtual potential temperature at 2 different time steps (day - 03/11/2015 - 1200 UTC, night - 01/13/2013 - 0900 UTC) at the North Sand Sea station. Dots: data from the ERA5 reanalysis. Dashed lines: boundary layer height given by the ERA5 reanalysis (Online Resource section 2). Plain lines: vertical (boundary layer) and linear (free atmosphere) fits to estimate the stratification properties. **c–f:** Sketches representing the interaction between the giant dunes and the atmospheric flow for different meteorological conditions. **g:** Streamlines over a sinusoidal topography $\xi(x, y)$ qualitatively representing the effect of low, medium and strong flow confinement, in relation to the above panels (see Appendix 1 for more details). The blue arrow indicates the undisturbed wind direction.

must then be considered (Fig. 7). First, topographic obstacles typically disturb the flow over a characteristic height similar to their length. As flow confinement is characterised by a thickness H , the interaction between the dunes and the wind in the ABL is well captured by the parameter kH . The height H is directly related to the radiative fluxes at the Earth surface. It is typically on the order of a kilometre, but significantly varies with the circadian and seasonal cycles. Emerging and small dunes, with wavelengths in the range 20 to 100 m, are not affected by the confinement, corresponding to $kH \gg 1$. For giant dunes with kilometric wavelengths, however, their interaction with the FA is significant (Andreotti et al. 2009). This translates into a parameter kH in the range 0.02–5, depending on the moment of the day and the season. A second important mechanism is associated with the existence of a thin intermediate so-called capping layer between the ABL and the FA. It is characterised by a density jump $\Delta\rho$, which controls the ‘rigidity’ of this interface, i.e. how much its deformation affects streamline compression. This is usually quantified using the Froude number (Vosper 2004; Stull 2006; Sheridan and Vosper 2006; Hunt et al. 2006; Jiang 2014):

$$\mathcal{F} = \frac{U}{\sqrt{\frac{\Delta\rho}{\rho_0} g H}}, \quad (1)$$

where U is the wind velocity at the top of the ABL and ρ_0 its average density. The intensity of the stratification, i.e. the amplitude of the gradient $|\partial_z \rho|$, also impacts its ability to deform the capping layer under the presence of an underlying obstacle, and thus affects the influence of flow confinement. This can be quantified using the internal Froude number (Vosper 2004; Stull 2006; Sheridan and Vosper 2006; Hunt et al. 2006; Jiang 2014) $\mathcal{F}_I = kU/N$, where $N = \sqrt{-g\partial_z \rho/\rho_0}$ is the Brunt-Väisälä frequency (Stull 1988). Both Froude numbers have in practice the same qualitative effect on flow confinement, and we shall restrict the main discussion to \mathcal{F} only.

With this theoretical framework in mind, and in the context of the measured wind data in the North and South Sand Sea stations, the smallest wind disturbances are expected to occur during the day, when the ABL depth is the largest and comparable to the dune wavelength ($kH \gtrsim 1$), which corresponds to a weak confinement situation (Fig. 7c,d). In contrast, large wind disturbances are expected to occur during the night, when the confinement is mainly induced by a shallow ABL (Fig. 7e). However, this strong confinement can be somewhat reduced in the case of strong winds, corresponding to large values of the Froude number and a less ‘rigid’ interface (Fig. 7f). This is in qualitative agreement with the transition from deflected to non-deflected winds related to low and high velocities observed in our data (Sec. 2.2).

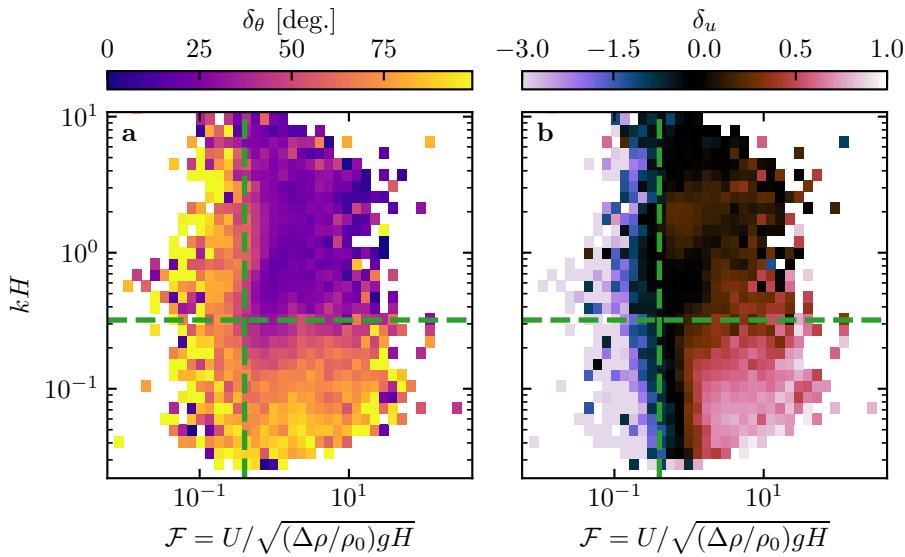


Fig. 8 Regime diagrams of the wind deviation δ_θ (a) and relative attenuation/amplification δ_u (b) in the space (\mathcal{F}, kH) , containing the data from both the North Sand Sea and South Sand Sea stations. Green dashed lines empirically delimit the different regimes. The point density in each bin of the diagrams is shown in Online Resource Fig. S10 – 95% of the data occur in the range $-1 < \delta_u < 1$. Similar regime diagrams in the spaces (\mathcal{F}_I, kH) and $(\mathcal{F}_I, \mathcal{F})$ are shown in Online Resource Fig. S11.

269 3.2 Data distribution in the flow regimes

270 We can go one step further and analyse how our data quantitatively spread
 271 over the different regimes discussed above. For that purpose, one needs to
 272 compute kH and \mathcal{F} from the time series. H , U and the other atmospheric
 273 parameters can be deduced from the various vertical profiles (temperature,
 274 humidity) available in the ERA5 climate reanalysis (Online Resource section
 275 2). We quantify the flow deflection δ_θ as the minimal angle between the wind
 276 orientations comparing the local measurements and the regional predictions.
 277 We also compute the relative velocity modulation as

$$\delta_u = \frac{u_*^{\text{ERA}} - u_*^{\text{station}}}{u_*^{\text{ERA}}}. \quad (2)$$

278 These two quantities are represented as maps in the plane (\mathcal{F}, kH) (Fig. 8a,b),
 279 and one can clearly identify different regions in these graphs. Small wind dis-
 280 turbances (small δ_θ and δ_u) are located in the top-right part of the diagrams,
 281 corresponding to a regime with low-interaction as well as low-confinement (kH
 282 and \mathcal{F} large enough, Fig. 7d). Lower values of kH (stronger interaction) or of
 283 Froude number (stronger confinement) both lead to an increase in wind dis-
 284 turbances, both in terms of orientation and velocity. Below a crossover value
 285 $kH \simeq 0.3$, wind disturbance is less sensitive to the \mathcal{F} -value. This is probably

due to enhanced non-linear effects linked to flow modulation by the obstacle when confinement is strong. The Froude number also controls a transition from damped to amplified wind velocities in the interdune, with a crossover around $\mathcal{F} \simeq 0.4$ (Fig. 8b). Such an amplification is rather unexpected. Checking the occurrence of the corresponding data, it appears that these amplifications are associated with the southerly sea breeze, and occur dominantly during the October–March period, when the other easterly wind is not present (Online Resource Fig. S12a–b). Furthermore, they occur less frequently during the afternoon, and more frequently at the end of the day (Online Resource Fig. S12c). This effect may be linked to a change in the flow behaviour in the lee side of the obstacles but further measurements are needed in order to assess the different possibilities (Baines 1995; Vosper 2004).

4 Discussion and conclusion

The feedback of the giant dunes on the wind flow has important implications for smaller scales bedforms. As illustrated in Fig. 9, small linear dunes (~ 50 m wide) are often present in the 1–2 km interdune between giant linear dunes in the Namib Sand Sea (Livingstone et al. 2010). These smaller dunes do not exhibit the same orientation as the large ones, and are sometimes named ‘crossing dunes’. Whilst differences between large and small scale dune patterns are observed ubiquitously, they are largely attributed to the presence of two different dune growth mechanisms, leading to two different dune patterns (orientations and/or morphologies) for the same wind regime (Courrech du Pont et al. 2014; Runyon et al. 2017; Lü et al. 2017; Song et al. 2019; Gadal et al. 2020; Hu et al. 2021). Here, however, our arguments enable the development of differing orientations for the small and giant linear dunes whilst also imposing the same dune growth mechanism (elongating mode). Figure 9 shows how the orientations for the small and giant dunes can be derived from the locally measured and regionally predicted winds respectively (red arrows in Fig. 9). These predictions require a specification for the threshold of eolian sand transport. Importantly, its value expressed as a shear velocity $u_{\text{th}} \simeq 0.15 \text{ ms}^{-1}$ is reached in the deflected wind regime already. The feedback of the giant dunes on the wind described in this study thus provides a potential explanation for the existence of these small linear dunes elongating across the interdune, a dynamic which has remained unresolved to date. These crossing dunes could provide additional constraints for the inference of local winds from bedforms, similarly to that currently performed on Mars using ripple orientations (Liu and Zimbelman 2015; Hood et al. 2021). Further work is needed to investigate these processes in more detail, including measurements of sediment transport and flow on the top of dunes.

This study presents the evidence that wind flow patterns around giant dunes are influenced by the atmospheric boundary layer, particularly during nocturnal conditions. It leaves open the debate as to whether the size of giant dunes is limited by the depth of this layer (Andreotti et al. 2009), in contrast to

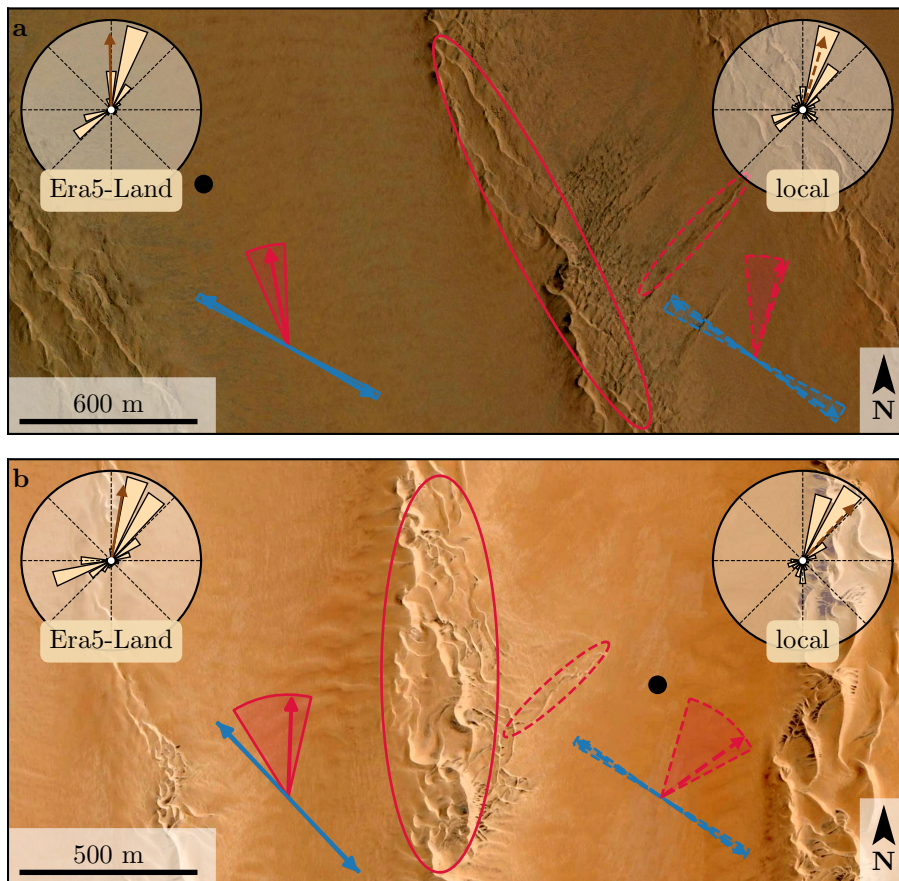


Fig. 9 Implications for smaller scale patterns in (a) the South Sand Sea and (b) North Sand Sea. The ellipses indicate the different types of elongating dunes, at large (plain line) and small (dashed line) scales. Dune orientation are predicted using the model of Courrech du Pont et al. (2014) from the sand flux angular distributions, shown here (roses and resultant transport direction) for typical values (grain size $180 \mu\text{m}$, flux-up ratio of 1.6). Code for corresponding arrows: use of ERA5-Land data (plain line), use of local measurements (dashed line), prediction for the bed instability growth mechanism (blue), prediction for the elongation growth mechanism (red). Wedges show the uncertainty on the orientation calculation when parameters are varied. The black dots indicate the location of the meteorological stations with respect to the dunes. See Appendix 2 for additional details.

329 an unconstrained dune growth, ever-slower with size (Gunn et al. 2021). More
 330 field evidence is needed from additional dune fields, but this mechanism would
 331 then allow for the inference of the ABL depth from giant bedform wavelengths
 332 where measurements are not feasible or available, such as Titan (Lorenz et al.
 333 2010).

334 To conclude on conditions under which the ERA5-Land reanalysis data can
 335 reliably be used to study dune morphodynamics, we summarise the compari-
 336 son of local (direct measurements) and regional (climate reanalysis) wind data.

In flat areas, the agreement between the two confirms the ability of the ERA5-Land climate reanalysis to predict the wind regime down to scales ~ 10 km, i.e the model grid. When smaller scale topographies are present (giant dunes in our case), locally measured winds can significantly differ from the regionally predicted ones. This is the case when the disturbances induced by the dunes interact with the lower part of the ABL vertical structure, which presents circadian variations. During the day, when the capping layer is typically high, this interaction is small, and the ERA5-Land predictions are also quantitatively consistent with the local data. During the night, however, the presence of a shallow atmospheric boundary layer induces a strong confinement of the flow, and is associated with large wind deflection by the dunes. Importantly, we find that this effect can be counterbalanced for large wind velocities, which are capable of deforming the capping layer, thus decreasing the influence of the confinement.

The theoretical computation of the wind disturbances induced by sinusoidal ridges under flow confinement has been performed in the linear limit (Andreotti et al. 2009, 2012), i.e. when the aspect ratio of these ridges is small ($k\xi_0 \ll 1$). These models are able to qualitatively reproduce the observed wind deflection (Appendix 1, Online Resource Figs. S11 and S13), and thus provide the physical support for the interpretation we propose here based on hydrodynamic regimes. However, these models cannot quantitatively predict the magnitude of these observations, probably due to the presence of expected non-linearities in high confinement situations linked to strong flow modulations. Besides, these linear calculations only predict wind attenuation in the interdune, in contrast with the observed enhanced velocities associated with particular evening winds from the South during the period October-March (Online Resource Fig. S12). Some other models predict different spatial flow structures in response to a modulated topography, such as lee waves and rotors (Baines 1995; Vosper 2004). However, our measurements are located at a single point in the interdune, so we are unable to explore these types of responses. Data at different places along and across the ridges are needed to investigate and possibly map such flow structures, and for further comparisons with the models.

Acknowledgements We would like to acknowledge the contributors of the following open-source python librairies, Matplotlib (Hunter 2007), Numpy (Harris et al. 2020) and Scipy (Virtanen et al. 2020), which provide an incredibly efficient ecosystem allowing scientific research in Python.

All data used in this study can be found in Gadal et al. (2022). Note that it contains modified Copernicus Climate Change Service Information (2021). Neither the European Commission nor ECMWF is responsible for any use that may be made of the Copernicus Information or Data it contains. Fully documented codes used to analyse this study are available at <https://github.com/Cgadal/GiantDunes> (will be made public upon acceptance of this manuscript for publication).

Multiple grants have supported the collection of wind data through visits to the four sites between 2013 and 2020 (John Fell Oxford University Press (OUP) Research Fund (121/474); National Geographic (CP-029R-17); Natural Environment Research Council UK (NE/R010196/1 and NE/H021841/1 NSFGEO-NERC); Southampton Marine and Maritime

384 Institute SMMI EPSRC-GCRF UK), along with research permits (1978/2014, 2140/2016,
 385 2304/2017, 2308/2017, RPIV00022018, RPIV0052018, RPIV00230218). The authors are
 386 very grateful for support from Etosha National Park (especially Shyane Kötting, Boas Er-
 387 ckie, Pierre du Preez, Claudine Cloete, Immanuel Kapofi, Wilferd Versfeld, and Werner
 388 Kilian), Gobabeb Namib Research Institute (Gillian Maggs-Kölling and Eugene Marais),
 389 The Skeleton Coast National Park (Joshua Kazzeurua). Various researchers and desert en-
 390 thusiasts have assisted with instruments and the logistics of expeditions, especially Mary
 391 Seely for expert guidance at the North Sand Sea site.

392 Finally, we acknowledge financial support from the Laboratoire d'Excellence UnivEarthS
 393 Grant ANR-10-LABX-0023, the Initiative d'Excellence Université de Paris Grant ANR-18-
 394 IDEX-0001, the French National Research Agency Grants ANR-17-CE01-0014/SONO and
 395 the National Science Center of Poland Grant 2016/23/B/ST10/01700.

396 **Appendix 1: Linear theory of wind response to topographic pertur-
 397 bation**

398 Following the work of Fourrière et al. (2010), Andreotti et al. (2012) and
 399 Andreotti et al. (2009), we briefly describe in this appendix the framework
 400 for the linear response of a turbulent flow to a topographic perturbation of
 401 small aspect ratio. As a general bed elevation can be decomposed into Fourier
 402 modes, we focus here on a sinusoidal topography:

$$\xi = \xi_0 \cos [k (\cos(\alpha)y - \sin(\alpha)x)], \quad (3)$$

403 which is also a good approximation for the giant dunes observed in the North
 404 Sand Sea and South Sand Sea Station (Fig. 2 and Online Resource Fig. S4).
 405 Here, x and y are the streamwise and spanwise coordinates, $k = 2\pi/\lambda$ the
 406 wavenumber of the sinusoidal perturbation, α its crest orientation with respect
 407 to the x -direction (anticlockwise) and ξ_0 its amplitude. The two components
 408 of the basal shear stress $\tau = \rho_0 u_* \mathbf{u}_*$, constant in the flat bottom reference
 409 case, can then be generically written as:

$$\tau_x = \tau_0 \left(1 + k \xi_0 \sqrt{\mathcal{A}_x^2 + \mathcal{B}_x^2} \cos [k (\cos(\alpha)y - \sin(\alpha)x) + \phi_x] \right), \quad (4)$$

$$\tau_y = \tau_0 k \xi_0 \sqrt{\mathcal{A}_y^2 + \mathcal{B}_y^2} \cos [k (\cos(\alpha)y - \sin(\alpha)x) + \phi_y], \quad (5)$$

410 where τ_0 is the reference basal shear stress on a flat bed. We have defined
 411 the phase $\phi_{x,y} = \tan^{-1}(\mathcal{B}_{x,y}/\mathcal{A}_{x,y})$ from the in-phase and in-quadrature hy-
 412 drodynamical coefficients $\mathcal{A}_{x,y}$ and $\mathcal{B}_{x,y}$. They are functions of k and of the
 413 flow conditions, i.e the bottom roughness, the vertical flow structure and the
 414 incident flow direction, and the theoretical framework developed in the above
 415 cited papers proposes methods to compute them in the linear regime.

⁴¹⁶ Following Andreotti et al. (2012), the effect of the incident wind direction
⁴¹⁷ can be approximated by the following expressions:

$$\mathcal{A}_x = \mathcal{A}_0 \sin^2 \alpha, \quad (6)$$

$$\mathcal{B}_x = \mathcal{B}_0 \sin^2 \alpha, \quad (7)$$

$$\mathcal{A}_y = -\frac{1}{2} \mathcal{A}_0 \cos \alpha \sin \alpha, \quad (8)$$

$$\mathcal{B}_y = -\frac{1}{2} \mathcal{B}_0 \cos \alpha \sin \alpha, \quad (9)$$

⁴¹⁸ where \mathcal{A}_0 and \mathcal{B}_0 are now two coefficients independent of the dune orientation
⁴¹⁹ α , corresponding to the transverse case ($\alpha = 90^\circ$). For a fully turbulent
⁴²⁰ boundary layer capped by a stratified atmosphere, these coefficients depend
⁴²¹ on kH , kz_0 , \mathcal{F} and \mathcal{F}_I (Andreotti et al. 2009). In this study, we assume a con-
⁴²² stant hydrodynamic roughness $z_0 \simeq 1$ mm (Online Resource section 1). For
⁴²³ the considered giant dunes, this leads to $kz_0 \simeq 2 \cdot 10^{-6}$, as their wavelength
⁴²⁴ is $\lambda \simeq 2.4$ km (or $k \simeq 2 \cdot 10^{-3} \text{ m}^{-1}$). Values of z_0 extracted from field data
⁴²⁵ indeed typically fall between 0.1 mm and 10 mm (Sherman and Farrell 2008;
⁴²⁶ Field and Pelletier 2018). Importantly, \mathcal{A}_0 and \mathcal{B}_0 do not vary much in the
⁴²⁷ corresponding range of kz_0 (Fourrière et al. 2010), and the results presented
⁴²⁸ here are robust with respect to this choice.

⁴²⁹ With capping layer height and Froude numbers computed from the ERA5-
⁴³⁰ Land time series, the corresponding \mathcal{A}_0 and \mathcal{B}_0 can be deduced, as displayed
⁴³¹ in Online Resource Fig. S13. Interestingly, it shows similar regimes as in the
⁴³² diagrams of Fig. 8 and Online Resource Fig. S11a,b, supporting the underly-
⁴³³ ing physics. However, the agreement is qualitative only. Further, the linearity
⁴³⁴ assumption of the theoretical framework requires $(|\tau| - \tau_0)/\tau_0 \ll 1$, which
⁴³⁵ translates into $k\xi\sqrt{\mathcal{A}_0^2 + \mathcal{B}_0^2} \ll 1$. In our case, the giant dune morphology
⁴³⁶ gives $k\xi_0 \simeq 0.1$, which means that one quits the regime of validity of the
⁴³⁷ linear theory when the coefficient modulus $\sqrt{\mathcal{A}_0^2 + \mathcal{B}_0^2}$ becomes larger than a
⁴³⁸ few units. In accordance with the theoretical expectations, these coefficients
⁴³⁹ present values on the order of unity ($\mathcal{A}_0 \simeq 3$ and $\mathcal{B}_0 \simeq 1$) in unconfined sit-
⁴⁴⁰ uations (Claudin et al. 2013; Lü et al. 2021). In contrast and as illustrated
⁴⁴¹ in Online Resource Fig. S13a,b, larger values are predicted in case of strong
⁴⁴² confinement, which does not allow us to proceed to further quantitative com-
⁴⁴³ parison with the data.

⁴⁴⁴ Finally, the linear model is also able to reproduce the enhancement of the
⁴⁴⁵ flow deflection over the sinusoidal ridges when $\sqrt{\mathcal{A}_0^2 + \mathcal{B}_0^2}$ is increased (Online
⁴⁴⁶ Resource Fig. S13). Here, using $k\xi_0 \simeq 0.1$ to be representative of the amplitude
⁴⁴⁷ of the giant dunes at the North Sand Sea station, the coefficient modulus is
⁴⁴⁸ bounded to 10.

449 Appendix 2: Sediment transport and dune morphodynamics

450 We summarise in this appendix the sediment transport and dune morphodynamics
 451 theoretical framework leading to the prediction of sand fluxes and dune
 452 orientations from wind data.

453 *Sediment transport* — The prediction of sand fluxes from wind data has been
 454 a long standing issue in aeolian geomorphological studies (Fryberger and Dean
 455 1979; Pearce and Walker 2005; Sherman and Li 2012; Shen et al. 2019). Based
 456 on laboratory studies in wind tunnels (Rasmussen et al. 1996; Iversen and
 457 Rasmussen 1999; Creyssels et al. 2009; Ho et al. 2011), as well as physical
 458 considerations (Ungar and Haff 1987; Andreotti 2004; Durán et al. 2011; Pähzt
 459 and Durán 2020), it has been shown that the steady saturated saltation flux
 460 over a flat sand bed depends linearly on the shear stress:

$$\frac{q_{\text{sat}}}{Q} = \Omega \sqrt{\Theta_{\text{th}}} (\Theta - \Theta_{\text{th}}), \quad (10)$$

461 where Ω is a proportionality constant, $Q = d\sqrt{(\rho_s - \rho_0)gd/\rho_0}$ is a character-
 462 istic flux, $\Theta = \rho_0 u_*^2 / (\rho_s - \rho_0)gd$ the Shields number, and Θ_{th} its threshold
 463 value below which saltation vanishes. $\rho_s = 2.6 \text{ g cm}^{-3}$ and $d = 180 \mu\text{m}$ are
 464 the grain density and diameter, and g is the gravitational acceleration. The
 465 shear velocity, and consequently the Shields number as well as the sediment
 466 flux, are time dependent.

467 Recently, Pähzt and Durán (2020) suggested an additional quadratic term
 468 in Shields to account for grain-grain interactions within the transport layer at
 469 strong wind velocities:

$$\frac{q_{\text{sat}, t}}{Q} = \frac{2\sqrt{\Theta_{\text{th}}}}{\kappa\mu} (\Theta - \Theta_{\text{th}}) \left(1 + \frac{C_M}{\mu} [\Theta - \Theta_{\text{th}}] \right), \quad (11)$$

470 where $\kappa = 0.4$ is the von Kármán constant, $C_M \simeq 1.7$ a constant and $\mu \simeq 0.6$ is
 471 a friction coefficient, taken to be the avalanche slope of the granular material.
 472 The fit of this law to the experimental data of Creyssels et al. (2009) and Ho
 473 et al. (2011) gives $\Theta_{\text{th}} = 0.0035$. The fit of Eq. 10 on these same data similarly
 474 gives $\Omega \simeq 8$ and $\Theta_{\text{th}} = 0.005$. The sand flux angular distributions and the
 475 dune orientations in Fig. 9 are calculated using this law (11). We have checked
 476 that using the ordinary linear relationship (10) instead does not change the
 477 predicted dune orientations by more than a few degrees.

478 *Dune orientations* — Dune orientations are predicted with the dimensional
 479 model of Courrech du Pont et al. (2014), from the sand flux time series com-
 480 puted with the above transport law. Two orientations are possible depending
 481 on the mechanism dominating the dune growth: elongation or bed instabil-
 482 ity. The orientation α corresponding the bed instability is then the one that
 483 maximises the following growth rate (Rubin and Hunter 1987):

$$\sigma \propto \frac{1}{H_d W_d T} \int_0^T q_{\text{crest}} |\sin(\theta - \alpha)| dt, \quad (12)$$

484 where θ is the wind orientation measured with respect to the same reference
 485 as α , and H_d and W_d are dimensional constants respectively representing the
 486 dune height and width. The integral runs over a time T , which must be repre-
 487 sentative of the characteristic period of the wind regime. The flux at the crest
 488 is expressed as:

$$q_{\text{crest}} = q_{\text{sat}} [1 + \gamma |\sin(\theta - \alpha)|], \quad (13)$$

489 where the flux-up ratio γ has been calibrated to 1.6 using field studies, under-
 490 water laboratory experiments and numerical simulations. Predictions of the
 491 linear analysis of Gadal et al. (2019) and Delorme et al. (2020) give similar
 492 results.

493 Similarly, the dune orientation corresponding to the elongation mechanism
 494 is the one that verifies:

$$\tan(\alpha) = \frac{\langle q_{\text{crest}}(\alpha) \mathbf{e}_\theta \rangle \cdot \mathbf{e}_{WE}}{\langle q_{\text{crest}}(\alpha) \mathbf{e}_\theta \rangle \cdot \mathbf{e}_{SN}}, \quad (14)$$

495 where $\langle \cdot \rangle$ denotes a vectorial time average. The unitary vectors \mathbf{e}_{WE} , \mathbf{e}_{SN} and
 496 \mathbf{e}_θ are in the West-East, South-North and wind directions, respectively.

497 The resulting computed dune orientations, blue and red arrows in Fig. 9,
 498 then depend on a certain number of parameters (grain properties, flux-up ratio,
 499 etc.), for which we take typical values for aeolian sandy deserts. Due to the lack
 500 of measurements in the studied places, some uncertainties can be expected. We
 501 therefore run a sensitivity test by calculating the dune orientations for grain
 502 diameters ranging from 100 μm to 400 μm and for a speed-up ratio between
 503 0.1 and 10 (wedges in Fig. 9).

504 References

- 505 Andreotti B (2004) A two-species model of aeolian sand transport. *J Fluid
506 Mech* 510:47–70
- 507 Andreotti B, Claudin P, Douady S (2002) Selection of dune shapes and veloc-
508 ities part 1: Dynamics of sand, wind and barchans. *The European Physical
509 Journal B-Condensed Matter and Complex Systems* 28(3):321–339
- 510 Andreotti B, Fourrière A, Ould-Kaddour F, Murray B, Claudin P (2009) Gi-
511 ant aeolian dune size determined by the average depth of the atmospheric
512 boundary layer. *Nature* 457:1120–1123
- 513 Andreotti B, Claudin P, Devauchelle O, Durán O, Fourrière A (2012) Bedforms
514 in a turbulent stream: ripples, chevrons and antidunes. *J Fluid Mech* 690:94–
515 128
- 516 Ashkenazy Y, Yizhaq H, Tsoar H (2012) Sand dune mobility under climate
517 change in the kalahari and australian deserts. *Climatic Change* 112:901–923
- 518 Baddock M, Livingstone I, Wiggs G (2007) The geomorphological significance
519 of airflow patterns in transverse dune interdunes. *Geomorphology* 87:322–
520 336
- 521 Baines PG (1995) Topographic effects in stratified flows. Cambridge university
522 press
- 523 Bauer BO, Sherman DJ, Wolcott JF (1992) Sources of uncertainty in shear
524 stress and roughness length estimates derived from velocity profiles. *The
525 Professional Geographer* 44:453–464
- 526 Belcher S, JCR H (1998) Turbulent flow over hills and waves. *Annu Rev Fluid
527 Mech* 30:507–538
- 528 Blumberg DG, Greeley R (1996) A comparison of general circulation model
529 predictions to sand drift and dune orientations. *J Clim* 9:3248–3259
- 530 Bristow NR, Best J, Wiggs GFS, Nield JM, Baddock MC, Delorme P, Chris-
531 tensen KT (2022) Topographic perturbation of turbulent boundary layers
532 by low-angle, early-stage aeolian dunes. *Earth Surf Process Landf* n/a(n/a),
533 DOI <https://doi.org/10.1002/esp.5326>
- 534 Brown S, Nickling WG, Gillies JA (2008) A wind tunnel examination of shear
535 stress partitioning for an assortment of surface roughness distributions. *J
536 Geophys Res* 113:F02S06
- 537 Charru F, Andreotti B, Claudin P (2013) Sand ripples and dunes. *Annu Rev
538 Fluid Mech* 45:469–493
- 539 Claudin P, Wiggs G, Andreotti B (2013) Field evidence for the upwind velocity
540 shift at the crest of low dunes. *Boundary-Layer Meteorol* 148:195–206
- 541 Claudin P, Durán O, Andreotti B (2017) Dissolution instability and roughen-
542 ing transition. *J Fluid Mech* 832:R2
- 543 Claudin P, Louge M, Andreotti B (2021) Basal pressure variations induced by
544 a turbulent flow over a wavy surface. *Frontiers in Physics* 9:682564
- 545 Courrech du Pont S (2015) Dune morphodynamics. *C R Phys* 16:118–138
- 546 Courrech du Pont S, Narteau C, Gao X (2014) Two modes for dune orientation.
547 *Geology* 42:743–746

- 548 Creyssels M, Dupont P, El Moctar AO, Valance A, Cantat I, Jenkins JT, Pasini
549 JM, Rasmussen KR (2009) Saltating particles in a turbulent boundary layer:
550 experiment and theory. *J Fluid Mech* 625:47–74
- 551 de Winter W, Donker J, Sterk G, Van Beem J, Ruessink G (2020) Regional
552 versus local wind speed and direction at a narrow beach with a high and
553 steep foredune. *Plos one* 15(1):e0226983
- 554 Dee DP, Uppala SM, Simmons AJ, Berrisford P, Poli P, Kobayashi S, Andrae
555 U, Balmaseda M, Balsamo G, Bauer dP, et al. (2011) The era-interim re-
556 analysis: Configuration and performance of the data assimilation system. *Q*
557 *J R Meteorol Soc* 137:553–597
- 558 Delorme P, Wiggs G, Baddock M, Claudin P, Nield J, Valdez A (2020) Dune
559 initiation in a bimodal wind regime. *J Geophys Res* 125:e2020JF005757
- 560 Durán O, Claudin P, Andreotti B (2011) On aeolian transport: Grain-scale
561 interactions, dynamical mechanisms and scaling laws. *Aeolian Res* 3:243–
562 270
- 563 Durran DR (1990) Mountain waves and downslope winds. In: *Atmospheric*
564 *processes over complex terrain*, Springer, pp 59–81
- 565 Farr TG, Rosen PA, Caro E, Crippen R, Duren R, Hensley S, Kobrick M,
566 Paller M, Rodriguez E, Roth L, et al. (2007) The shuttle radar topography
567 mission. *Rev Geophys* 45
- 568 Fernando H, Mann J, Palma J, Lundquist JK, Barthelmie RJ, Belo-Pereira M,
569 Brown W, Chow F, Gerz T, Hocut C, et al. (2019) The perdigão: Peering
570 into microscale details of mountain winds. *Bull Am Meteorol Soc* 100:799–
571 819
- 572 Field JP, Pelletier JD (2018) Controls on the aerodynamic roughness length
573 and the grain-size dependence of aeolian sediment transport. *Earth Surf*
574 *Process Landf* 43:2616–2626
- 575 Finnigan J, Raupach M, Bradley E, Aldis G (1990) A wind tunnel study
576 of turbulent flow over a two-dimensional ridge. *Boundary-Layer Meteorol*
577 50:277–317
- 578 Finnigan J, Ayotte K, Harman I, Katul G, Oldroyd H, Patton E, Poggi D,
579 Ross A, Taylor P (2020) Boundary-layer flow over complex topography.
580 *Boundary-Layer Meteorol* 177:247–313
- 581 Flack K, Schultz M (2010) Review of hydraulic roughness scales in the fully
582 rough regime. *Journal of Fluids Engineering* 132:041203
- 583 Fourrière A, Claudin P, Andreotti B (2010) Bedforms in a turbulent stream:
584 formation of ripples by primary linear instability and of dunes by nonlinear
585 pattern coarsening. *J Fluid Mech* 649:287–328
- 586 Frederick KA, Hanratty TJ (1988) Velocity measurements for a turbulent non-
587 separated flow over solid waves. *Exp Fluids* 6:477–486
- 588 Fryberger SG, Dean G (1979) Dune forms and wind regime. A study of global
589 sand seas 1052:137–169
- 590 Gadal C, Narteau C, Courrech Du Pont S, Rozier O, Claudin P (2019) Incip-
591 ient bedforms in a bidirectional wind regime. *J Fluid Mech* 862:490–516
- 592 Gadal C, Narteau C, Courrech du Pont S, Rozier O, Claudin P (2020) Peri-
593 odicity in fields of elongating dunes. *Geology* 48:343–347

- 594 Gadal C, Delorme P, Narteau C, Wiggs G, Baddock M, Nield JM, Claudin
595 P (2022) Data used in 'Local wind regime induced by giant linear dunes:
596 comparison of ERA5-Land re-analysis with surface measurements'. DOI
597 10.5281/zenodo.6343138
- 598 Garvey B, Castro IP, Wiggs G, Bullard J (2005) Measurements of flows over
599 isolated valleys. *Boundary-Layer Meteorol* 117(3):417–446
- 600 Gong W, Ibbetson A (1989) A wind tunnel study of turbulent flow over model
601 hills. *Boundary-Layer Meteorol* 49:113–148
- 602 Gong W, Taylor P, Dörnbrack A (1996) Turbulent boundary-layer flow over
603 fixed aerodynamically rough two-dimensional sinusoidal waves. *J Fluid Mech*
604 312:1–37
- 605 Gunn A, Casasanta G, Di Liberto L, Falcini F, Lancaster N,
606 Jerolmack DJ (2021) What sets aeolian dune height? DOI
607 <https://doi.org/10.31223/X5QG8S>
- 608 Harris CR, Millman KJ, van der Walt SJ, Gommers R, Virtanen P, Cournapeau D, Wieser E, Taylor J, Berg S, Smith NJ, et al. (2020) Array program-
609 ming with numpy. *Nature* 585:357–362
- 610 Hersbach H, Bell B, Berrisford P, Hirahara S, Horányi A, Muñoz-Sabater J,
611 Nicolas J, Peubey C, Radu R, Schepers D, et al. (2020) The era5 global
612 reanalysis. *Q J R Meteorol Soc* 146:1999–2049
- 613 Hesp PA, Hastings K (1998) Width, height and slope relationships and aero-
614 dynamic maintenance of barchans. *Geomorphology* 22(2):193–204
- 615 Hesp PA, Smyth TAG, Nielsen P, Walker IJ, Bauer BO, Davidson-Arnott R
616 (2015) Flow deflection over a foredune. *Geomorphology* 230:64–74
- 617 Ho TD, Valance A, Dupont P, Ould El Moctar A, Tuan Duc H, Valance A,
618 Dupont P, Ould El Moctar A (2011) Scaling laws in aeolian sand transport.
619 *Phys Rev Lett* 106:4–7
- 620 Hood DR, Ewing RC, Roback KP, Runyon K, Avouac JP, McEnroe M (2021)
621 Inferring airflow across martian dunes from ripple patterns and dynamics.
622 *Frontiers in Earth Science* 9:702828
- 623 Howard AD (1977) Effect of slope on the threshold of motion and its applica-
624 tion to orientation of wind ripples. *Geological Society of America Bulletin*
625 88:853–856
- 626 Hu Z, Gao X, Lei J, Zhou N (2021) Geomorphology of aeolian dunes in the
627 western sahara desert. *Geomorphology* 392:107916
- 628 Hunt J, Leibovich S, Richards K (1988) Turbulent shear flows over low hills.
629 *Q J R Meteorol Soc* 114:1435–1470
- 630 Hunt JCR, Vilenski GG, Johnson ER (2006) Stratified separated flow around
631 a mountain with an inversion layer below the mountain top. *J Fluid Mech*
632 556:105–119
- 633 Hunter JD (2007) Matplotlib: A 2d graphics environment. *Computing in sci-
634 ence & engineering* 9:90–95
- 635 Iversen JD, Rasmussen KR (1999) The effect of wind speed and bed slope on
636 sand transport. *Sedimentology* 46:723–731
- 637 Jackson PS, Hunt JCR (1975) Turbulent wind flow over a low hill. *Q J R
638 Meteorol Soc* 101:929–955
- 639

- 640 Jiang Q (2014) Applicability of reduced-gravity shallow-water theory to atmo-
641 spheric flow over topography. *J Atmos Sci* 71:1460–1479
- 642 Jolivet M, Braucher R, Dovchintseren D, Hocquet S, Schmitt J, ASTER Team
643 (2021) Erosion around a large-scale topographic high in a semi-arid sedimentary basin: Interactions between fluvial erosion, aeolian erosion and aeolian
644 transport. *Geomorphology* 386:107747
- 645 Kim HG, Patel VC, Lee CM (2000) Numerical simulation of wind flow over
646 hilly terrain. *J Wind Eng Ind Aerodyn* 87:45–60
- 647 Lancaster J, Lancaster N, Seely M (1984) Climate of the central namib desert.
648 Madoqua 1984:5–61
- 649 Lancaster N (1985) Winds and sand movements in the namib sand sea. *Earth
650 Surf Process Landf* 10:607–619
- 651 Lancaster N, Nickling W, Neuman CM, Wyatt V (1996) Sediment flux and
652 airflow on the stoss slope of a barchan dune. *Geomorphology* 17(1-3):55–62
- 653 Lewis HW, Mobbs SD, Lehning M (2008) Observations of cross-ridge flows
654 across steep terrain. *Q J R Meteorol Soc* 134:801–816
- 655 Liu ZYC, Zimbelman JR (2015) Recent near-surface wind directions inferred
656 from mapping sand ripples on martian dunes. *Icarus* 261:169–181
- 657 Livingstone I, Warren A (2019) Aeolian geomorphology: a new introduction.
658 Wiley
- 659 Livingstone I, Bristow C, Bryant RG, Bullard J, White K, Wiggs GFS, Baas
660 ACW, Bateman MD, Thomas DSG (2010) The namib sand sea digital
661 database of aeolian dunes and key forcing variables. *Aeolian Res* 2:93–104
- 662 Lorenz R, Claudin P, Andreotti B, Radebaugh J, Tokano T (2010) A 3 km
663 atmospheric boundary layer on titan indicated by dune spacing and huygens
664 data. *Icarus* 205:719–721
- 665 Lü P, Narteau C, Dong Z, Rozier O, Du Pont SC (2017) Unravelling raked
666 linear dunes to explain the coexistence of bedforms in complex dunefields.
667 Nature communications 8:1–9
- 668 Lü P, Narteau C, Dong Z, Claudin P, Rodriguez S, An Z, Fernandez-Cascales
669 L, Gadal C, Courrech du Pont S (2021) Direct validation of dune instability
670 theory. *Proceedings of the National Academy of Sciences* 118
- 671 Mason P, Sykes R (1979) Flow over an isolated hill of moderate slope. *Q J R
672 Meteorol Soc* 105:383–395
- 673 McKenna Neuman C, Lancaster N, Nickling WG (1997) Relations between
674 dune morphology, air flow, and sediment flux on reversing dunes, Sil-
675 ver Peak, Nevada. *Sedimentology* 44(6):1103–1111, DOI 10.1046/j.1365-
676 3091.1997.d01-61.x
- 677 Muñoz-Sabater J, Dutra E, Agustí-Panareda A, Albergel C, Arduini G, Bal-
678 samo G, Boussetta S, Choulga M, Harrigan S, Hersbach H, et al. (2021)
679 Era5-land: A state-of-the-art global reanalysis dataset for land applications.
680 *Earth Syst Sci Data* 13:4349–4383
- 681 Nield JM, King J, Wiggs GFS, Leyland J, Bryant RG, Chiverrell RC, Darby
682 SE, Eckhardt FD, Thomas DSG, Vircavs LH, Washington R (2014) Esti-
683 mating aerodynamic roughness over complex surface terrain. *J Geophys Res*
684 118:12948–12961
- 685

- 686 Nield JM, Wiggs GF, Baddock MC, Hipondoka MH (2017) Coupling leeside
687 grainfall to avalanche characteristics in aeolian dune dynamics. *Geology*
688 45(3):271–274
- 689 Pähzt T, Durán O (2020) Unification of aeolian and fluvial sediment transport
690 rate from granular physics. *Phys Rev Lett* 124:168001
- 691 Pearce KI, Walker IJ (2005) Frequency and magnitude biases in the 'Fryberger'
692 model, with implications for characterizing geomorphically effective winds.
693 *Geomorphology* 68:39–55
- 694 Pelletier JD, Field JP (2016) Predicting the roughness length of turbulent flows
695 over landscapes with multi-scale microtopography. *Earth Surface Dynamics*
696 4:391–405
- 697 Poggi D, Katul G, Albertson J, Ridolfi L (2007) An experimental investigation
698 of turbulent flows over a hilly surface. *Phys Fluids* 19:036601
- 699 Rasmussen KR, Iversen JD, Rautaheimo P (1996) Saltation and wind flow
700 interaction in a variable slope wind tunnel. *Geomorphology* 17:19–28
- 701 Raupach M (1992) Drag and drag partition on rough surfaces. *Boundary-Layer
702 Meteorol* 60:375–395
- 703 Rubin DM, Hunter RE (1987) Bedform alignment in directionally varying
704 flows. *Science* 237:276–278
- 705 Runyon K, Bridges N, Ayoub F, Newman C, Quade J (2017) An integrated
706 model for dune morphology and sand fluxes on mars. *Earth and Planetary
707 Science Letters* 457:204–212
- 708 Sauermann G, Andrade Jr J, Maia L, Costa U, Araújo A, Herrmann H (2003)
709 Wind velocity and sand transport on a barchan dune. *Geomorphology* 54(3–
710 4):245–255
- 711 Seidel DJ, Zhang Y, Beljaars A, Golaz JC, Jacobson AR, Medeiros B (2012)
712 Climatology of the planetary boundary layer over the continental united
713 states and europe. *J Geophys Res* 117:D17106
- 714 Shao Y (2008) Physics and modelling of wind erosion, vol 37. Springer Science
715 & Business Media
- 716 Shen Y, Zhang C, Huang X, Wang X, Cen S (2019) The effect of wind speed
717 averaging time on sand transport estimates. *Catena* 175:286–293
- 718 Sheridan PF, Vosper SB (2006) A flow regime diagram for forecasting lee
719 waves, rotors and downslope winds. *Meteorol Appl* 13:179–195
- 720 Sherman D, Farrell E (2008) Aerodynamic roughness lengths over movable
721 beds: Comparison of wind tunnel and field data. *J Geophys Res* 113:1–10
- 722 Sherman DJ, Li B (2012) Predicting aeolian sand transport rates: A reevalu-
723 ation of models. *Aeolian Res* 3:371–378
- 724 Smith AB, Jackson DWT, Cooper JAG (2017) Three-dimensional airflow and
725 sediment transport patterns over barchan dunes. *Geomorphology* 278:28–42
- 726 Song Q, Gao X, Lei J, Li S (2019) Spatial distribution of sand dunes and their
727 relationship with fluvial systems on the southern margin of the taklimakan
728 desert, china. *Geomatics, Natural Hazards and Risk* 10:2408–2428
- 729 Spalding DB (1961) A single formula for the law of the wall. *Journal of Applied
730 Mechanics* 28:455–458

- 731 Stull R (2006) 9 - the atmospheric boundary layer. In: Wallace JM, Hobbs PV
732 (eds) *Atmospheric Science* (Second Edition), second edition edn, Academic
733 Press, San Diego, pp 375–417
- 734 Stull RB (1988) An introduction to boundary layer meteorology, vol 13.
735 Springer Science & Business Media
- 736 Sullivan PP, McWilliams JC (2010) Dynamics of winds and currents coupled
737 to surface waves. *Annu Rev Fluid Mech* 42:19–42
- 738 Sykes RI (1980) An asymptotic theory of incompressible turbulent boundary-
739 layer flow over a small hump. *J Fluid Mech* 101:647–670
- 740 Taylor P, Teunissen H (1987) The Askervein hill project: overview and back-
741 ground data. *Boundary-Layer Meteorol* 39:15–39
- 742 Taylor P, Mason P, Bradley E (1987) Boundary-layer flow over low hills.
743 *Boundary-Layer Meteorol* 39:107–132
- 744 Ungar JE, Haff PK (1987) Steady state saltation in air. *Sedimentology* 34:289–
745 299
- 746 Unsworth C, Parsons D, Hardy R, Reesink A, Best J, Ashworth P, Keevil G
747 (2018) The impact of nonequilibrium flow on the structure of turbulence
748 over river dunes. *Water Resour Res* 54:6566–6584
- 749 Uppala SM, Källberg P, Simmons AJ, Andrae U, Bechtold VDC, Fiorino M,
750 Gibson J, Haseler J, Hernandez A, Kelly G, et al. (2005) The era-40 re-
751 analysis. *Q J R Meteorol Soc* 131:2961–3012
- 752 Valance A, Rasmussen K, Ould El Moctar A, Dupont P (2015) The physics
753 of aeolian sand transport. *C R Phys* 16:1–13
- 754 Virtanen P, Gommers R, Oliphant TE, Haberland M, Reddy T, Cournapeau
755 D, Burovski E, Peterson P, Weckesser W, Bright J, et al. (2020) Scipy 1.0:
756 fundamental algorithms for scientific computing in python. *Nature methods*
757 17:261–272
- 758 Vogelezang D, Holtslag A (1996) Evaluation and model impacts of alternative
759 boundary-layer height formulations. *Boundary-Layer Meteorol* 81:245–269
- 760 Vosper SB (2004) Inversion effects on mountain lee waves. *Q J R Meteorol Soc*
761 130:1723–1748
- 762 Walker I, Davidson-Arnott R, Bauer B, Hesp P, Delgado-Fernandez I, Oller-
763 head J, Smyth T (2017) Scale-dependent perspectives on the geomorphology
764 and evolution of beach-dune systems. *Earth-Science Review* 171:220–253
- 765 Walker IJ, Nickling WG (2002) Dynamics of secondary airflow and sediment
766 transport over and in the lee of transverse dunes. *Prog Phys Geogr* 26(1):47–
767 75
- 768 Walker IJ, Hesp PA, Davidson-Arnott RG, Bauer BO, Namikas SL, Ollerhead
769 J (2009) Responses of three-dimensional flow to variations in the angle of
770 incident wind and profile form of dunes: Greenwich dunes, prince edward
771 island, canada. *Geomorphology* 105:127–138
- 772 Weaver C, Wiggs G (2011) Field measurements of mean and turbulent airflow
773 over a barchan sand dune. *Geomorphology* 128:32–41
- 774 Wiggs G, Bullard J, Garvey B, Castro I (2002) Interactions between airflow
775 and valley topography with implications for aeolian sediment transport.
776 *Physical Geography* 23:366–380

- 777 Zhang C, Li Q, Zhou N, Zhang J, Kang L, Shen Y, Jia W (2016) Field obser-
778 vations of wind profiles and sand fluxes above the windward slope of a sand
779 dune before and after the establishment of semi-buried straw checkerboard
780 barriers. *Aeolian Res* 20:59–70
- 781 Zilker DP, Hanratty TJ (1979) Influence of the amplitude of a solid wavy wall
782 on a turbulent flow. part 2. separated flows. *J Fluid Mech* 90:257–271
- 783 Zilker DP, Cook GW, Hanratty TJ (1977) Influence of the amplitude of a solid
784 wavy wall on a turbulent flow. part 1. non-separated flows. *J Fluid Mech*
785 82:29–51

786 **Local wind regime induced by giant linear dunes**
 787 — Supplementary Material —

788 **C. Gadal* · P. Delorme · C. Narteau · G.F.S. Wiggs · M. Baddock ·**
 789 **J.M. Nield · P. Claudin**

790

791 * Institut de Mécanique des Fluides de Toulouse, Université de Toulouse Paul
 792 Sabatier, CNRS, Toulouse INP-ENSEEIHT, Toulouse, France.

793 cyril.gadal@imft.fr

794 **1. Shear velocity and calibration of the hydrodynamical roughness**

795 As the regionally predicted and locally measured velocities are available at
 796 different heights, we can not compare them directly. We therefore convert all
 797 velocities into shear velocities u_* , characteristic of the turbulent velocity profile
 798 (Spalding 1961; Stull 1988):

$$\frac{u(z)}{u_*} = \frac{1}{\kappa} \ln \left(\frac{z}{z_0} \right), \quad (15)$$

799 where z is the vertical coordinate, $\kappa = 0.4$ the von Kármán constant and z_0 the
 800 hydrodynamic roughness. Several measurements of hydrodynamic roughnesses
 801 are available (Raupach 1992; Bauer et al. 1992; Brown et al. 2008; Nield et al.
 802 2014). In the absence of sediment transport, it is governed by the geometric
 803 features of the bed (Flack and Schultz 2010; Pelletier and Field 2016). When
 804 aeolian saltation occurs, it is rather controlled by the altitude of Bagnold's
 805 focal point (Durán et al. 2011; Valance et al. 2015), which depends on the
 806 wind velocity and grain properties (Sherman and Farrell 2008; Zhang et al.
 807 2016; Field and Pelletier 2018). Whether associated with geometric features
 808 or with sediment transport, its typical order of magnitude is the millimetre
 809 scale on sandy surfaces.

810 We do not have precise velocity vertical profiles to be able to deduce an
 811 accurate value of z_0 in the various environments of the meteorological stations
 812 (vegetated, arid, sandy). Our approach is to rather select the hydrodynamic
 813 roughness which allows for the best possible matching between the regionally
 814 predicted and locally measured winds, i.e. minimising the relative difference δ
 815 between the wind vectors of both datasets:

$$\delta = \frac{\sqrt{\langle \| \mathbf{u}_{*,\text{era}} - \mathbf{u}_{*,\text{station}} \|^2 \rangle}}{\sqrt{\langle \| \mathbf{u}_{*,\text{era}} \|^2 \rangle \langle \| \mathbf{u}_{*,\text{station}} \|^2 \rangle}}, \quad (16)$$

816 where $\langle \cdot \rangle$ denotes time average. This parameter is computed for values of z_0
 817 in ERA5-Land analysis ranging from 10^{-5} m to 10^{-2} m for the four different
 818 stations. Note that for the North Sand Sea and South Sand Sea stations, where
 819 the giant dunes feedback presumably affect the wind, we take into account the
 820 non-deflected winds only in the calculation of δ (with a 15° tolerance).

As shown in Online Resource Fig. S3, the minimum values of δ in the space $(z_0^{\text{ERA5Land}}, z_0^{\text{local}})$ form a line. We thus set the roughness in the ERA5-Land analysis to the typical value $z_0 = 10^{-3}$ m, and deduce the corresponding ones for the local stations. It leads to 2.7, 0.8, 0.1 and 0.5 mm for the Etosha West, North Sand Sea, Huab and South Sand Sea stations, respectively. Importantly, this approach somewhat impacts the calculation of the shear velocities, but not that of the wind directions. As such, most of our conclusions are independent of such a choice. However, it may affect the magnitude of the wind velocity attenuation/amplification in flow confinement situations.

2. Computation of the ABL characteristics

The estimation of the non-dimensional numbers associated with the ABL requires the computation of representative meteorological quantities. In arid areas, the vertical structure of the atmosphere can be approximated by a well mixed convective boundary layer of height H , topped by the stratified free atmosphere (Stull 1988; Shao 2008). In this context, one usually introduces the virtual potential temperature T_{vp} , which is a constant T_0 inside the boundary layer, and increases linearly in the FA (Online Resource Fig. S8a):

$$T_{\text{vp}}(z) = \begin{cases} T_0 & \text{for } z \leq H, \\ T_0 \left(1 + \frac{\Delta T_{\text{vp}}}{T_0} + \frac{N^2}{g}(z - H) \right) & \text{for } z \geq H, \end{cases} \quad (17)$$

where ΔT_{vp} is the temperature discontinuity at the capping layer and $N = \sqrt{g\partial_z T_{\text{vp}}/T_0}$ is the Brunt-Väisälä frequency, characteristic of the stratification. Note that, under the usual Boussinesq approximation, temperature and air density variations are simply related by $\delta T_{\text{vp}}/T_0 \simeq -\delta\rho/\rho_0$ (see Online Resource of Andreotti et al. (2009)), so that N can equivalently be defined from the density gradient as next to (1).

The ERA5 dataset provides vertical profiles of the geopotential ϕ , the actual temperature T and the specific humidity η at given pressure levels P . The vertical coordinate is then calculated as:

$$z = \frac{\phi R_t}{g R_t - \phi}, \quad (18)$$

where $R_t = 6371229$ m is the reference Earth radius and $g = 9.81$ m s⁻² is the gravitational acceleration. One also computes the virtual potential temperature as:

$$T_{\text{vp}} = T \left[1 + \left(\frac{M_d}{M_w} - 1 \right) \eta \right] \left(\frac{P_0}{P} \right)^{R/C_p}, \quad (19)$$

where $P_0 = 10^5$ Pa is the standard pressure, $R = 8.31$ J/K is the ideal gas constant, $C_p \simeq 29.1$ J/K is the air molar heat capacity, and $M_w = 0.018$ kg/Mol

and $M_d = 0.029 \text{ kg/Mol}$ are the molecular masses of water and dry air respectively. The specific humidity is related to the vapour pressure p_w as

$$\eta = \frac{\frac{M_w}{M_d} p_w}{p - \left(1 - \frac{M_w}{M_d}\right) p_w}. \quad (20)$$

The ERA5 dataset also provides an estimate of the ABL depth H , based on the behaviour of the Richardson vertical profile. This dimensionless number is defined as the ratio of buoyancy and flow shear terms, and can be expressed as $\text{Ri} = N^2 / (\partial_z u)^2$. It vanishes in the lower well-mixed layer where T_{vp} is constant, and increases in the stratified FA. Following the method and calibration of Vogelegang and Holtslag (1996); Seidel et al. (2012), the value $\text{Ri}(z) \simeq 0.25$ has been shown to be a good empirical criterion to give $z \simeq H$ within a precision varying from 50% for the shallower ABL (e.g. at night) to 20% for situations of stronger convection.

Examples of vertical profiles of the virtual potential temperature deduced from ERA5 are shown in Online Resource Fig. S8a. For each of them, an average temperature is computed below the ABL depth ($z < H$), and a linear function is fitted above, allowing us to extract the temperature jump ΔT_{vp} . Importantly, some profiles display a vertical structure that cannot be approximated by the simple form (17) used here (Online Resource Fig. S8b). In practice, we removed from the analysis all of those leading to the unphysical case $\Delta T_{\text{vp}} < 0$. We have noticed that these ‘ill-processed’ profiles dominantly occur in winter and are evenly spread across the hours of the day. Importantly, they represent $\simeq 12\%$ of the data only (Online Resource Fig. S8c,d), and we are thus confident that this data treatment does not affect our conclusions.

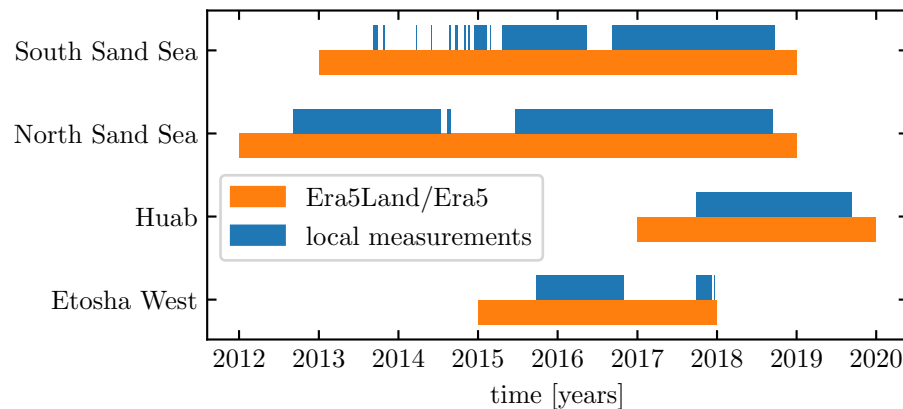


Fig. S1 Gant chart representing the valid time steps for the two data sets, for all stations.

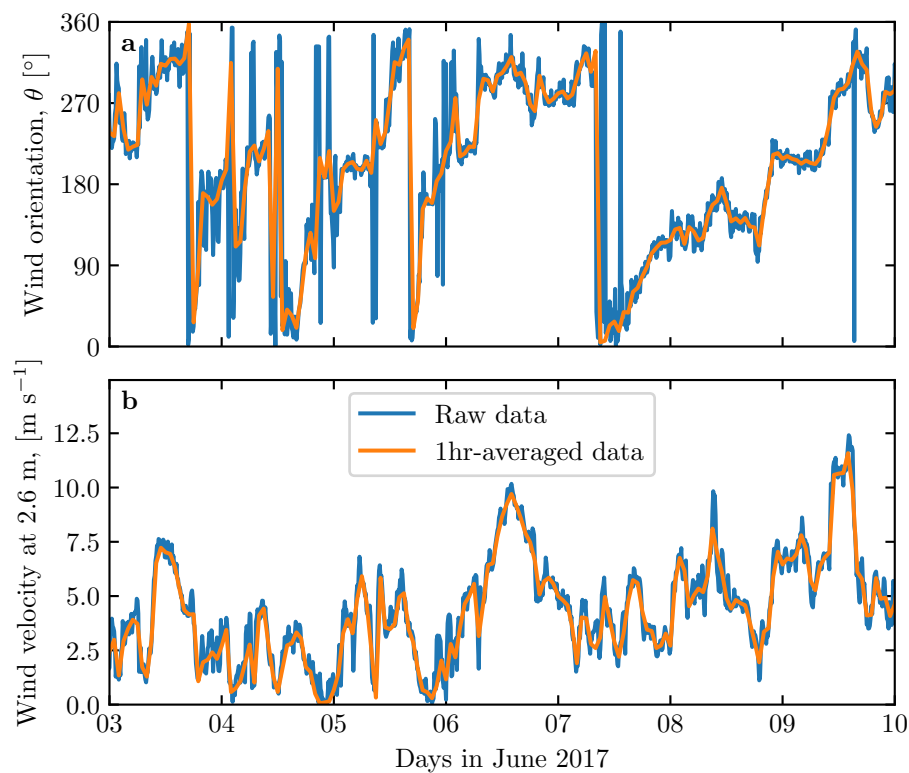


Fig. S2 Comparison between raw local wind measurements, and hourly-averaged data for South Sand Sea station. **a:** wind direction. **b:** wind velocity at height 2.6 m.

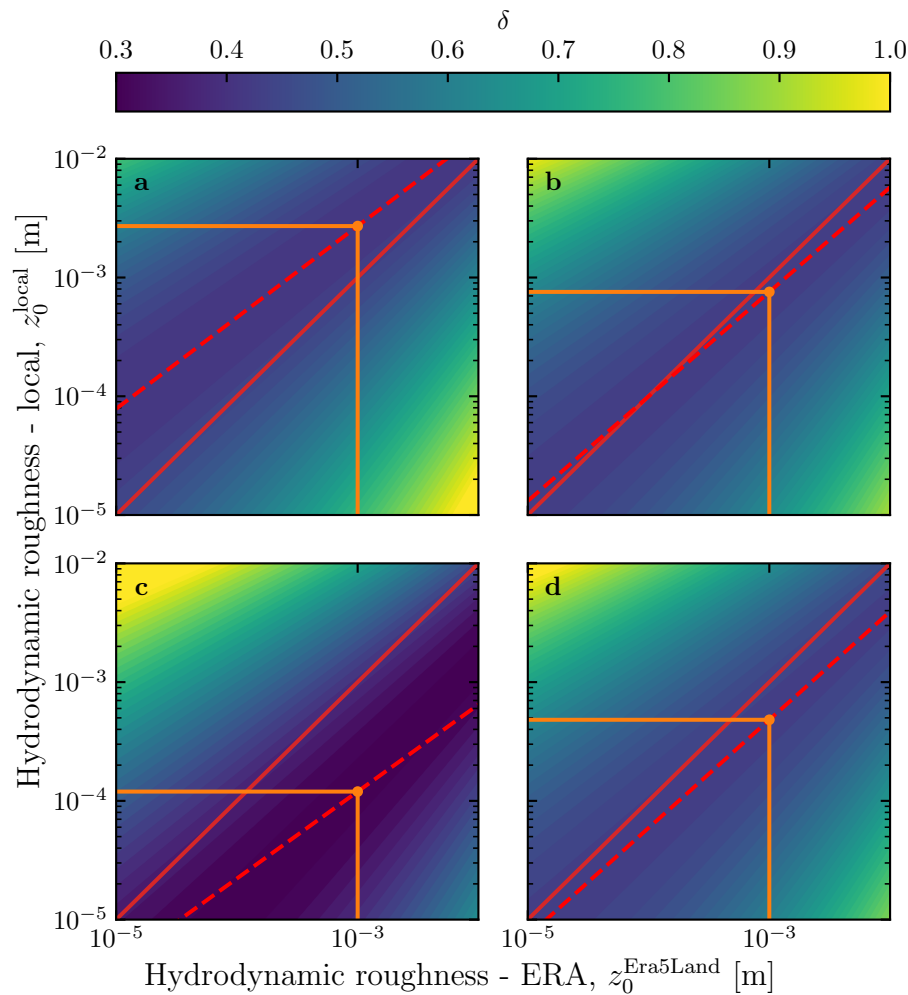


Fig. S3 Calibration of hydrodynamic roughness. The parameter δ (16) quantifying the difference between local and predicted winds is shown in colorscale as a function of the hydrodynamic roughnesses chosen for the ERA5-Land and for local winds, for the (a) Etosha West, (b) North Sand Sea, (c) Huab and (d) South Sand Sea stations. The red dashed and plain lines shows the minima of δ and the identity line, respectively. The orange lines and dots highlight the chosen hydrodynamic roughnesses for the local winds deduced from setting $z_0^{\text{ERA5Land}} = 1 \text{ mm}$.

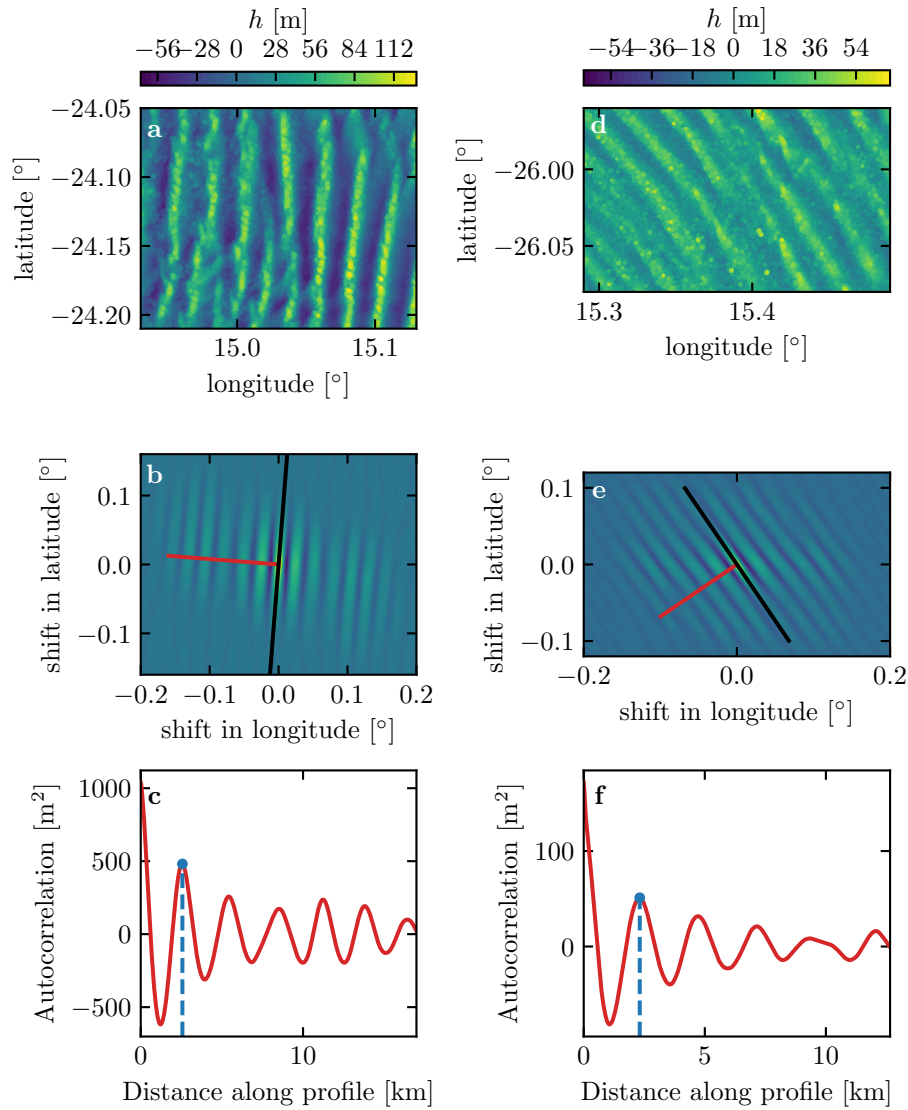


Fig. S4 Analysis of the DEMs of the North Sand Sea (left column – panels **a**, **b**, **c**) and South Sand Sea (right column – panels **d**, **e**, **f**) stations. **a–d**: Bed elevation detrended by a fitted second order polynomial base-line. **b–e**: Autocorrelation matrix shown in colorscale. The black line shows the detected dune orientation, and the red line represents the autocorrelation profile along which the dune wavelength is calculated, displayed in **c–f**. The blue lines and dots show the first peak of the autocorrelation profile, whose abscissa gives the characteristic wavelength of the dune pattern.

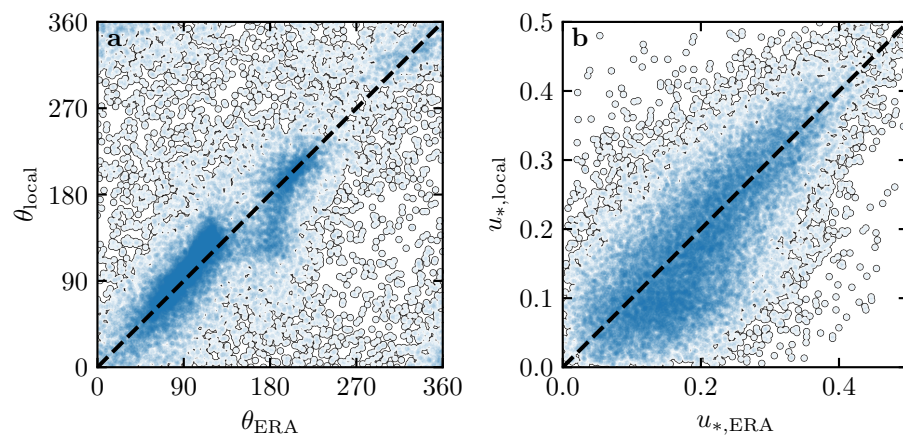


Fig. S5 Statistical comparison of the wind orientation (a) and velocity (b) between the ERA5-Land dataset and the local measurements for the Huab and Etosha West stations. Data point clustering around identity lines (dashed and black) provide evidence for agreement of the two sets.

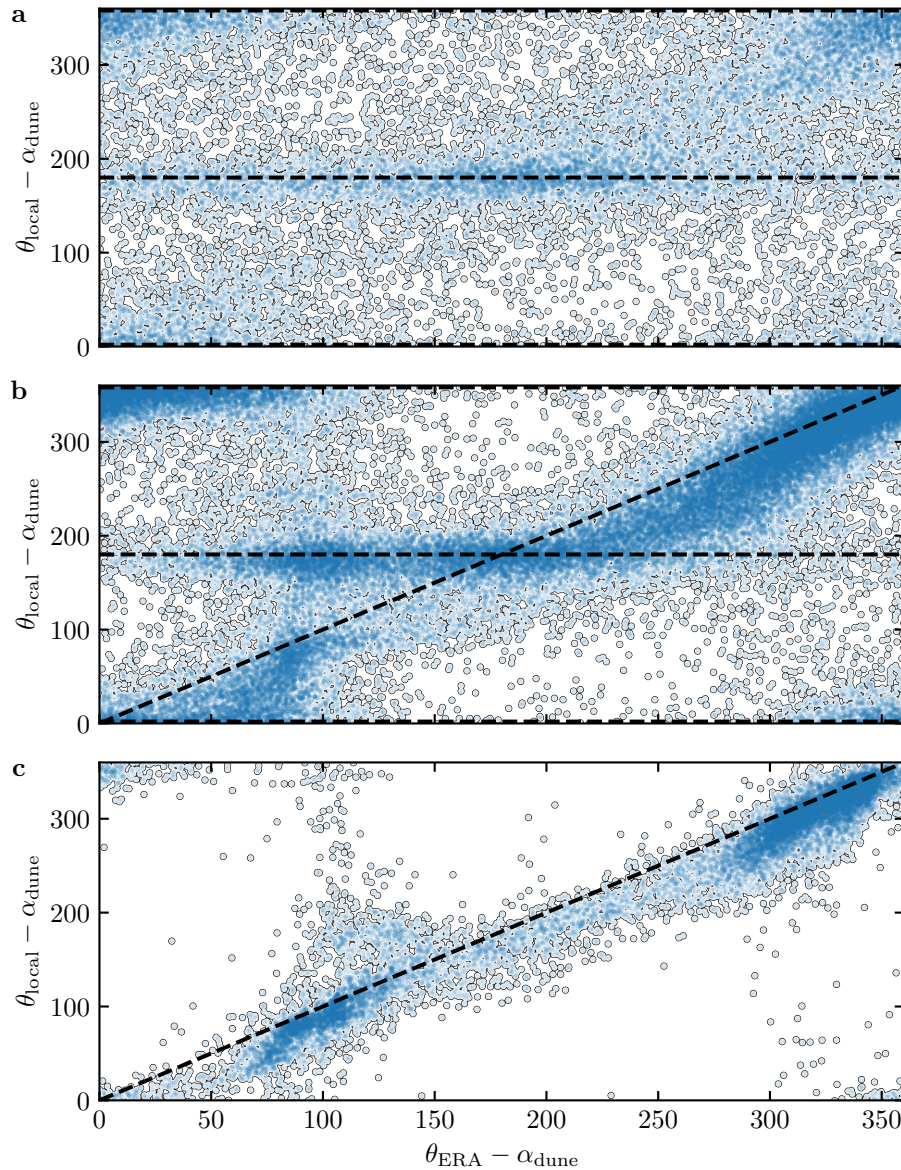


Fig. S6 Statistical comparison of the wind orientation between the ERA5-Land dataset and the local measurements for the South Sand Sea and North Sand Sea stations, for different velocity ranges. **a:** $u_{*,\text{ERA}} < 0.1 \text{ m s}^{-1}$. **b:** $0.1 < u_{*,\text{ERA}} \leq 0.25 \text{ m s}^{-1}$. **c:** $u_{*,\text{ERA}} \geq 0.25 \text{ m s}^{-1}$. The measured dune orientations are subtracted to the wind orientation, which allows us to plot both stations on the same graph. Black dashed lines indicate locally measured orientations aligned with the dune crests (here 0°, 180° and 360° – panels a, b), as well as the identity lines (panels b, c).

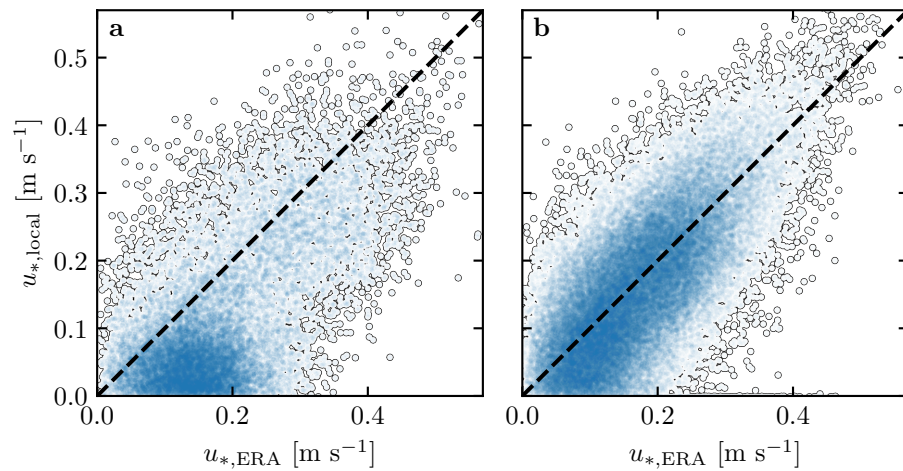


Fig. S7 Statistical comparison of the wind velocity between the ERA5-Land dataset and the local measurements for the South Sand Sea and North Sand Sea stations. **a:** Nocturnal summer easterly wind. **b:** Diurnal southerly wind. Black dashed lines are identity lines. The angle ranges used to select diurnal and nocturnal summer winds are the same as those in Figs. 4 and Figs. 6 of the main article.

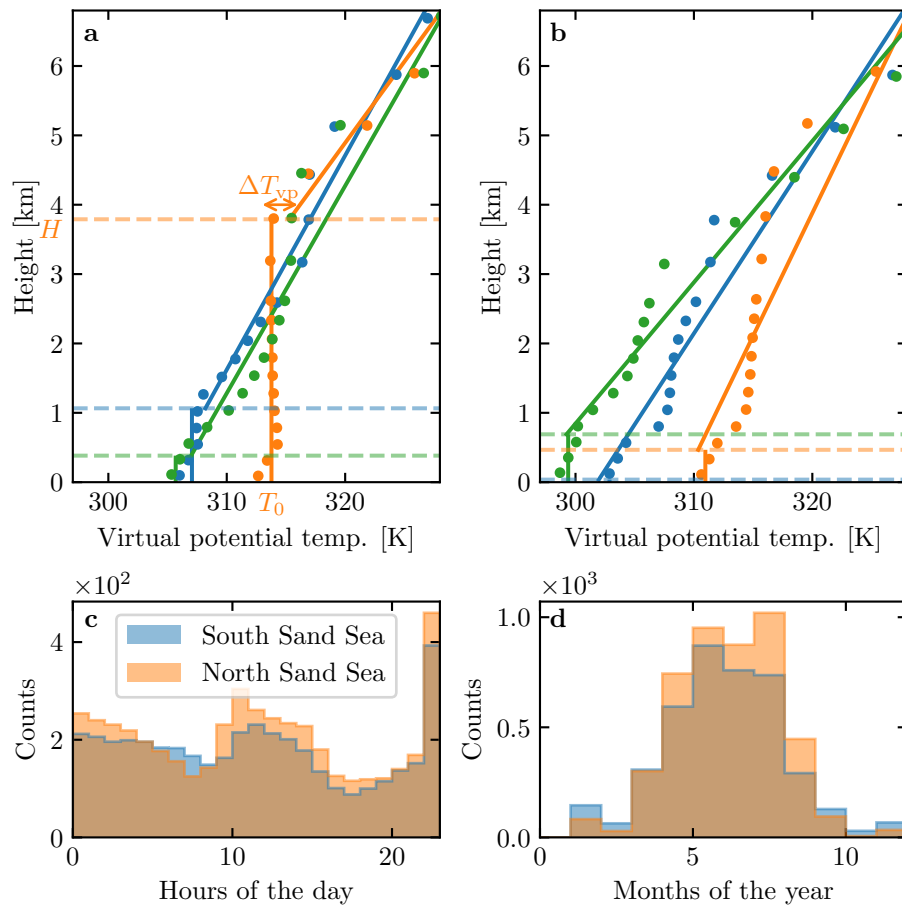


Fig. S8 **a:** Vertical profiles of the virtual potential temperature at three different times (blue: 29/11/2012 - 1100 UTC, orange: 21/03/2017 - 1200 UTC, green: 21/03/2017 - 2000 UTC) at the South Sand Sea station. Dots: data from the ERA5 reanalysis. Dashed lines: boundary layer height given by the ERA5 reanalysis. Plain lines: vertical (ABL) and linear (FA) fits to estimate the quantities displayed in Online Resource Fig. S9. **b:** Examples of ill-processed vertical profiles at three different times (blue: 2/12/2013 - 2300 UTC, orange: 20/03/2017 - 0000 UTC, green: 14/07/2017 - 1400 UTC) at the South Sand Sea station. **c:** Hourly distribution of ill-processed vertical profiles. **d:** Monthly distribution of ill-processed vertical profiles.

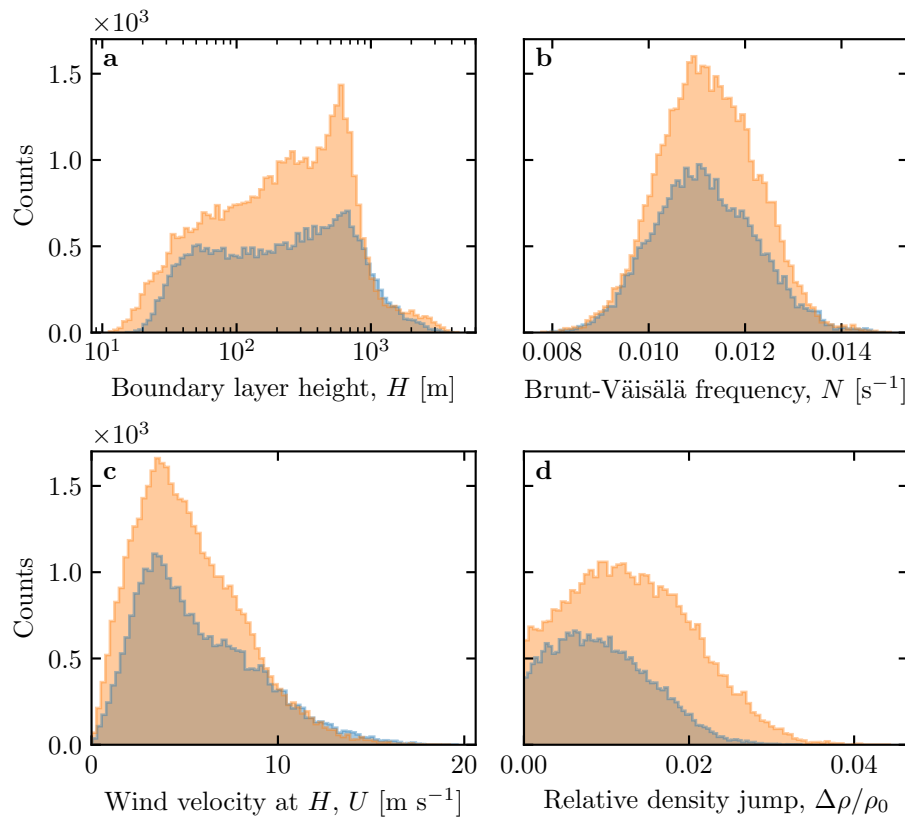


Fig. S9 Distributions of the meteorological parameters resulting from the processing of the ERA5-Land data for the South Sand Sea (blue) and the North Sand Sea (orange) stations.

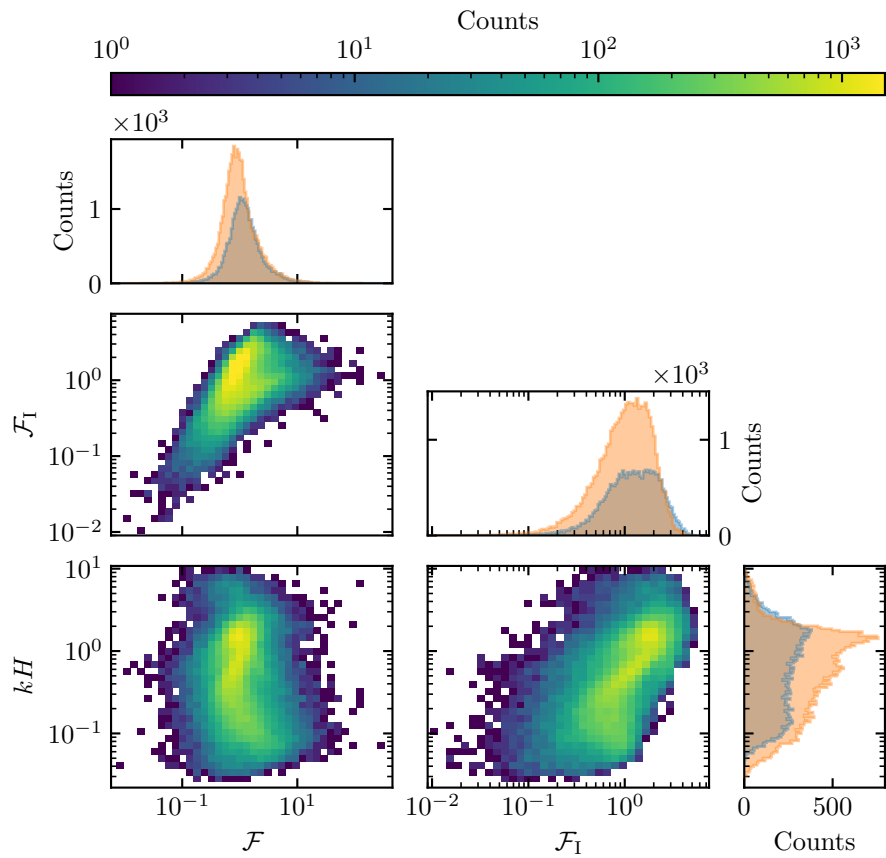


Fig. S10 Non-dimensional parameters distributions. For the marginal distributions, the orange correspond to the South Sand Sea station, and the blue to the North Sand Sea station.

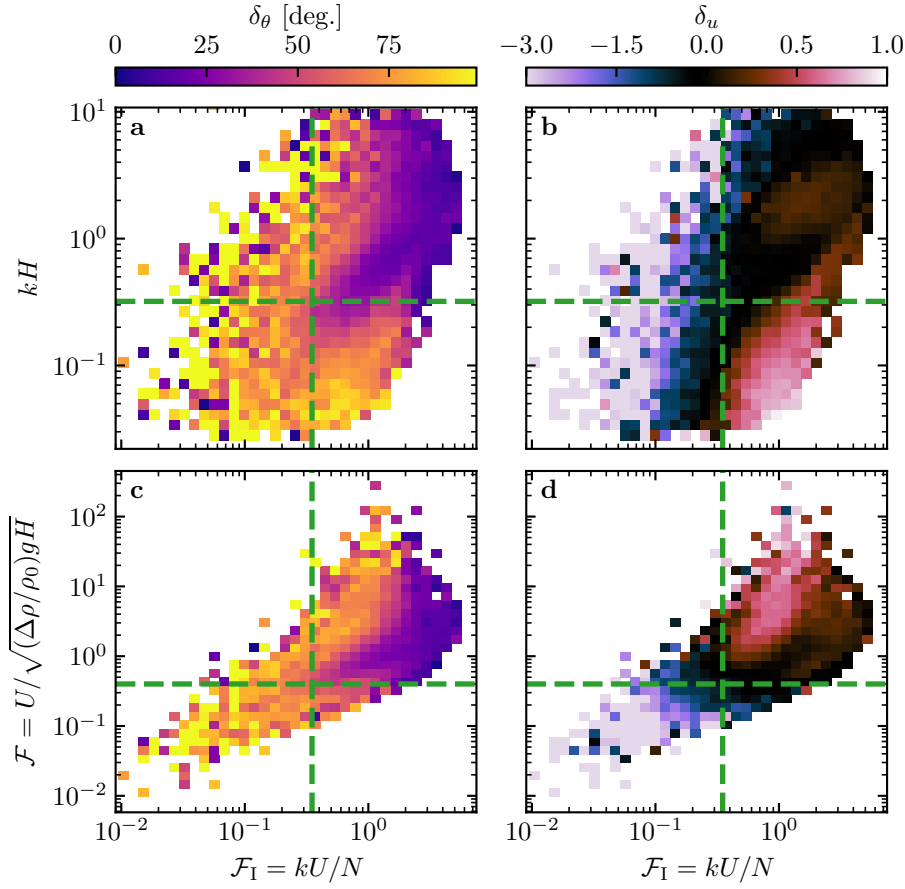


Fig. S11 Regime diagrams of the wind deviation δ_θ and relative attenuation/amplification δ_u in the spaces (\mathcal{F}_I, kH) and $(\mathcal{F}_I, \mathcal{F})$, containing the data from both the North Sand Sea and South Sand Sea stations. Green dashed lines empirically delimit the different regimes. The point density in each bin of the diagrams is shown in Online Resource Fig. S10 – 95% of the data occur in the range $-1 < \delta u < 1$. The similar regime diagrams in the space (\mathcal{F}, kH) are shown in Fig. 8.

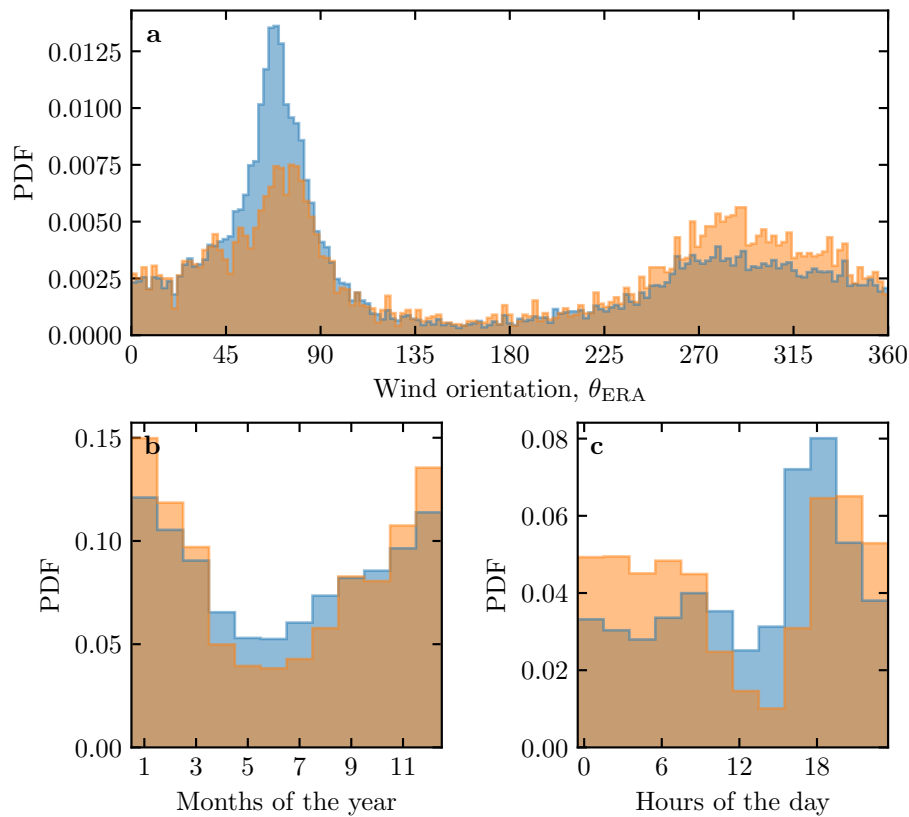


Fig. S12 Normalized distributions of amplified velocities for the North Sea (blue: $\delta_u < 0$, orange: $\delta_u < -0.5$). **a:** Angular distributions. **b:** Monthly distributions. **c:** Hourly distributions.

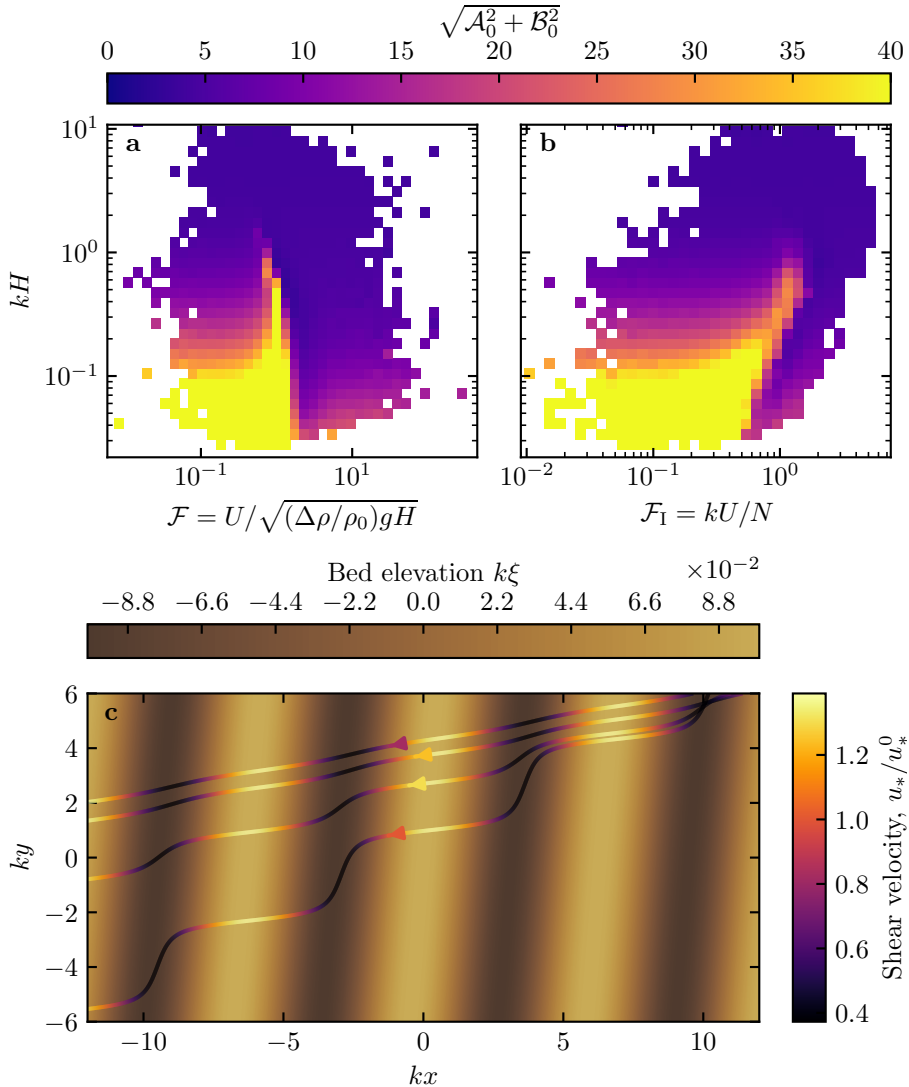


Fig. S13 Computation of the flow disturbance with the linear model of Andreotti et al. (2009). **a–b:** Magnitude of the hydrodynamic coefficients A_0 and B_0 , calculated from the time series of the non-dimensional numbers corresponding to the ERA5-Land wind data and ERA5 data on vertical pressure levels. **c** Shear velocity streamlines over sinusoidal ridges of amplitude $k\xi_0 = 0.1$ and for increasing values of $\sqrt{A_0^2 + B_0^2}$. From the upper to the lower streamline, values of $(kH, \mathcal{F}, \mathcal{F}_I, A_0, B_0, \sqrt{A_0^2 + B_0^2})$ are $(1.9, 0.6, 1.5, 3.4, 1.0, 3.5)$, $(1.5, 0.3, 0.4, 4.8, 1.4, 5.0)$, $(0.1, 3.5, 1.0, 8.6, 0.1, 8.6)$, $(0.5, 0.05, 0.04, 9.6, 2.5, 9.9)$.

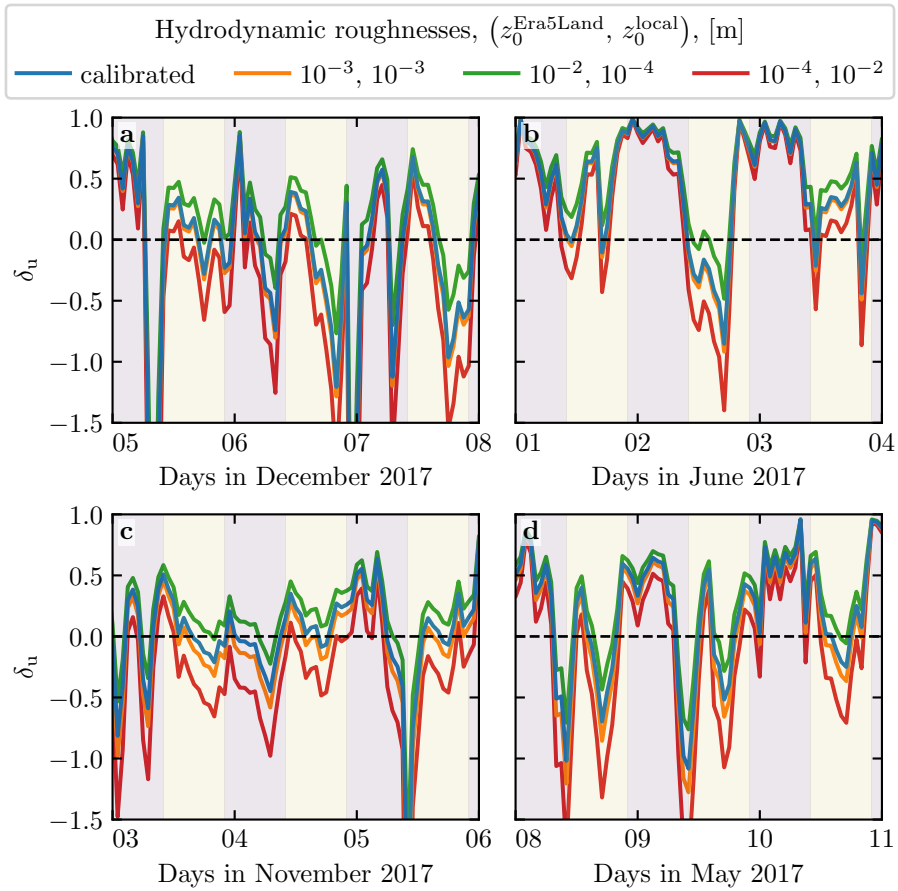


Fig. S14 Time series of the relative velocity disturbance δ_u corresponding to Fig. 5, for different values of the hydrodynamic roughnesses. **a:** North Sand Sea – summer, **b:** North Sand Sea – winter, **d:** South Sand Sea – summer, **e:** South Sand Sea – winter. Note that δ_θ is independent of the choice of z_0^{Era5Land} and z_0^{local} .